ISSN No. 0737-5352-70

Remote Sensing of Water Vapor over Land Using the Advanced Microwave Sounding Unit

Matthew J. Nielsen
Thomas H. Vonder Haar

Research was supported in part by Cloud Sat at NASA-Goddard under Contract Agreement NAS5-99237, the DoD Center for Geosciences/Atmospheric Research at Colorado State University under the Cooperative Agreement DAAD19-02-2-0005 with the Army Research Lab, and by the Joint Center for Satellite Data Assimilation (JCSDA) Program via NOAA grant NA17RJ1228#15 under CIRA's Cooperative Agreement with NOAA.

CIRA Cooperative Institute for Research in the Atmosphere

Center for Geosciences/Atmospheric Research

Colorado State University

THESIS

REMOTE SENSING OF WATER VAPOR OVER LAND USING THE ADVANCED MICROWAVE SOUNDING UNIT

Submitted by

Matthew J. Nielsen

Department of Atmospheric Science

In partial fulfillment of the requirements

For the Degree of Master of Science

Colorado State University

Fort Collins, Colorado

Fall 2005

ABSTRACT OF THESIS

REMOTE SENSING OF WATER VAPOR OVER LAND USING THE ADVANCED MICROWAVE SOUNDING UNIT

Water vapor is a fundamentally important variable in the atmosphere for making accurate forecasts. Its global distribution is a challenge to determine and can change rapidly in both space and time. Several ground and space based methods are currently employed to determine its spatial and temporal variability.

The microwave spectrum is very useful for remote sensing due to its ability to penetrate through clouds at most frequencies. Microwave satellite sensors have been used to retrieve atmospheric state parameters for several decades, however the retrievals of certain parameters have not been performed satisfactorily over land thus far. Retrievals rely on the ability to extract the atmospheric state from the upwelling radiation, most of which comes from emission from the surface. Knowing the surface emissivity to a high degree of accuracy is essential for calculating the land surface temperature, however it is also important because this emission must be removed in order to retrieve the atmospheric parameters desired. Land type, vegetation, snow, ice, rain, urbanization effects, and many other factors have an effect on the aggregate emission within each viewing scene and results in a strong sensitivity and variability of microwave emissivity on small scales.

A physically based iterative optimal estimation retrieval has been implemented to retrieve atmospheric parameters from the Advanced Microwave Sounding Unit (AMSU). This retrieval is based on the method of Engelen and Stephens (1999). The retrieval uses a first guess of water vapor and temperature profiles (currently from radiosondes, but will soon be from GDAS), and uses a first guess of emissivity at each of five frequencies (from the MEM). The retrieval was run with a highly accurate first guess in order to detect bias, and the total precipitable water amounts were validated against a radiosonde match-up dataset. The match-up showed fair agreement between the radiosondes and the retrieval (within 20%), however a systematic bias was detected due mostly to coastline contamination. Data from the Global Positioning System (GPS) was also used to validate the total precipitable water, however the results showed less agreement than the radiosonde results (variations of ~20-35%). Most of this disagreement stemmed from geographical co-location differences.

The analytical Jacobian was also examined to determine the sensitivities of all channels to the state vector parameters. This enables any retrieval user to pick a channel configuration that gives the desired sensitivities. Vertical profiles of water vapor sensitivities at four varying emissivities were investigated. Sensitivities of water vapor to emissivity were also examined at three distinct atmospheric pressure levels. The Jacobian determined that water vapor is able to be detected throughout a vertical column with adequate skill, although problematic areas occurred between 600 and 800 mb as the emissivity approached unity ($\varepsilon>0.99$) for a wet atmospheric case. These results give confidence that AMSU can detect TPW over land for both

weather forecasting and for climate studies. The current capabilities may be improved further once bias sources are dealt with satisfactorily.

Matthew J. Nielsen
Atmospheric Science Department
Colorado State University
Fort Collins, CO 80523
Fall 2005

Acknowledgements

I would like to thank my advisor, Dr. Thomas H. Vonder Haar, along with my committee members Dr. Christian Kummerow and Dr. V. Chandrasekar. Their advice, suggestions, and time have been greatly appreciated.

I extend special appreciation to many of the scientists from the Cooperative Institute for Research in the Atmosphere (CIRA) for all of their guidance and help, especially John Forsythe, Andy Jones, Phil Stephens, Ron Kessler, Phil Shott, and Cindy Combs.

I would also like to thank the members of the Vonder Haar research group, including Kevin Donofrio, Dustin Rapp, Kate Maclay, Becca Mazur, Holli Knutson, Kimberly Mueller, Cathy Meyer, and Curtis Seaman. Thanks also to Laura Sample and Kyle Leesman for their aide in programming and editing.

This work was supported in part by CloudSAT at NASA-Goddard under contract agreement NAS5-99237, the DoD Center for Geosciences/Atmospheric Research at Colorado State University under the Cooperative Agreement DAAD19-02-2-0005 with the Army Research Laboratory, and by the Joint Center for Satellite Data Assimilation (JCSDA) program via NOAA grant NA17RJ1228#15 under CIRA's cooperative agreement with NOAA.

TABLE OF CONTENTS

CHAPTER 1: INTRODUCTION **1**

1.1 WATER VAPOR 1
1.2 MICROWAVE REMOTE SENSING 4
1.3 SCIENTIFIC OBJECTIVES 8

CHAPTER 2: MICROWAVE REMOTE SENSING OVER LAND **13**

2.1 RADIATIVE TRANSFER 13
2.2 TRANSMITTANCE 13
2.3 THERMAL EMISSION 15
2.4 ATMOSPHERIC ABSORPTION 17
2.5 SURFACE EFFECTS-EMISSIVITY IMPACTS 18
2.6 NEW METHODS FOR A FIRST GUESS OF EMISSIVITY: THE MICROWAVE EMISSIVITY MODEL (MEM) 19
2.7 THE RADIATIVE TRANSFER EQUATION 21

CHAPTER 3: DATA SOURCES AND SPECIAL PROCESSING **26**

3.1 THE ADVANCED MICROWAVE SOUNDING UNIT-B 26
3.2 ANTENNA PATTERN CORRECTION FOR AMSU-B 29
3.3 THE GLOBAL POSITIONING SYSTEM 35

CHAPTER 4: WATER VAPOR RETRIEVAL **46**

4.1 AN INTRODUCTION TO INVERSE PROBLEMS 46
4.2 THE FORWARD RADIATIVE TRANSFER MODEL 49
4.3 OPTIMAL ESTIMATION 50
4.4 C1DOE RETRIEVAL 52

CHAPTER 5: SENSITIVITES **55**

5.1 THE ANALYTICAL JACOBIAN 55

CHAPTER 6: RESULTS AND CONCLUSIONS **72**

6.1 RESULTS 72
6.2 CONCLUSIONS 76
6.3 FUTURE WORK 79

REFERENCES **85**

LIST OF FIGURES

Figure 1.1: Monthly averaged column water vapor values from NVAP. As can be seen, water vapor is highly variable, even over monthly averages.

Figure 1.2: Transmittance in the microwave spectrum. There are two oxygen absorption features (near 60 and 118 GHz) and two water vapor absorption features (near 22 and 183 GHz).

Figure 2.1: Examples of the structure of the Planck Function, both as a function of frequency and wavelength.

Figure 2.2: An example image of global emissivity from the Microwave Emissivity Model (MEM). Courtesy of A. Jones, CIRA.

Figure 3.1: Measured NOAA-15 AMSU-B mainbeam and widebeam antenna efficiencies along with their corresponding frequency.

Figure 3.2: A schematic of a typical antenna gain pattern. The mainbeam is defined as 1.25 times the 3 db width. The near and far sidelobes are jointly referred to as the sidelobe.

Figure 3.3: A physical representation of the "Earth Disk" that the satellite sees.

Figure 3.4: The antenna pattern corrections for AMSU-B channel 16. Corrections are constant for view angles less than 28. Above this, the earth begins to become subtended by the satellite platform.

Figure 3.5: Effect of AMSU-B APC on surface emissivity, temperature and mixing ratio retrievals.

Figure 3.6: A global map of plate velocities. Most velocities are less than about 2 cm/yr (Rothacher, 2005).

Figure 3.7: Scalar precipitable water is obtained by averaging vector zenith-mapped slant delays.

Figure 3.8: A map of the GPS stations over CONUS.

Figure 4.1: The current data flow through the C1DOE algorithm.

Figure 4.2: The correlation matrix used in the C1DOE retrieval (McKague et al., 2001; McKague et al., 2003).

Figure 5.1: An example case of the Jacobian matrix. Null values are denoted in pink. Units of the Jacobian are in (K/K) for all temperatures, (K/(g/kg)) for mixing ratio, and (K) for emissivity.

Figure 5.2: The temperature profile for the "dry" case.

Figure 5.3: The mixing ratio profile for the "dry" case.

Figure 5.4: The temperature profile for the "wet" case.

Figure 5.5: The mixing ratio profile for the "wet" case.

Figure 5.6: The Jacobian vertical profiles for six frequencies (23.8, 55.5, 89, 150, 183+/-7 GHz, and 183+/-3 GHz for the dry atmospheric case with an emissivity of 0.5.

Figure 5.7: the Jacobian vertical profiles for five frequencies (23.8, 89, 150, 183+/-7 GHz, and 183+/-3 GHz) for the wet atmospheric case with an emissivity of 0.5.

Figure 5.8: The Jacobian vertical profiles for five frequencies (23.8, 89, 150, 183+/-7 GHz, and 183+/-3 GHz) for the dry atmospheric case with an emissivity of 0.7.

Figure 5.9: The Jacobian vertical profiles for five frequencies (23.8, 89, 150, 183+/-7 GHz, and 183+/-3 GHz) for the wet atmospheric case with an emissivity of 0.7.

Figure 5.10: The Jacobian vertical profiles for five frequencies (23.8, 89, 150, 183+/-7 GHz, and 183+/-3 GHz) for the dry atmospheric case with an emissivity of 0.9.

Figure 5.11: The Jacobian vertical profiles for five frequencies (23.8, 89, 150, 183+/-7 GHz, and 183+/-3 GHz) for the wet atmospheric case with an emissivity of 0.9.

Figure 5.12: The Jacobian vertical profiles for five frequencies (23.8, 89, 150, 183+/-7 GHz, and 183+/-3 GHz) for the dry atmospheric case with an emissivity of 0.99.

Figure 5.13: The Jacobian vertical profiles for five frequencies (23.8, 89, 150, 183+/-7 GHz, and 183+/-3 GHz) for the wet atmospheric case with an emissivity of 0.99.

Figure 5.14: The change in the Jacobian for five frequencies (23.8, 89, 150, 183+/-7 GHz, and 183+/-3 GHz) at 100 mb as the emissivity is increased from 0.5 to 1.0 for the dry case.

Figure 5.15: The change in the Jacobian for four frequencies (23.8, 89, 150, and 183+/-7 GHz) at 100 mb as the emissivity is increased from 0.5 to 1.0 for the wet case.

Figure 5.16: The change in the Jacobian for four frequencies (23.8, 89, 150, and 183+/-7 GHz) at 500 mb as the emissivity is increased from 0.5 to 1.0 for the dry case.

Figure 5.17: The change in the Jacobian for four frequencies (23.8, 89, 150, and 183+/-7 GHz) at 500 mb as the emissivity is increased from 0.5 to 1.0 for the wet case.

Figure 5.18: The change in the Jacobian for four frequencies (23.8, 89, 150, and 183+/-7 GHz) at 1000 mb as the emissivity is increased from 0.5 to 1.0 for the dry case.

Figure 5.19: The change in the Jacobian for four frequencies (23.8, 89, 150, and 183+/-7 GHz) at 1000 mb as the emissivity is increased from 0.5 to 1.0 for the wet case.

Figure 5.20: The corresponding NEΔT values for all AMSU channels.

Figure 6.1: A global map of the radiosonde and retrieval match-up data locations.

Figure 6.2: A plot of the radiosonde TPW versus the retrieved TPW. Units are in millimeters (mm).

Figure 6.3: A plot of the radiosonde TPW versus the retrieved TPW for only coastline data points. Units are in millimeters (mm).

Figure 6.4: A plot of the radiosonde TPW versus the retrieved TPW for only non-coastline data points. Units are in millimeters (mm).

Figure 6.5: A plot of the GPS TPW versus the retrieved TPW. Units are in millimeters (mm).

Figure 6.6: A plot of the radiosonde and retrieval RMS difference (in mm).

Figure 6.7: A histogram of the retrieved emissivities.

CHAPTER 1: INTRODUCTION

1.1 Water Vapor

Water vapor is a fundamentally important variable in the atmosphere for both climate studies and numerical weather forecasting. Numerous studies have confirmed that water vapor is not only one of the most powerful greenhouse gases present in the atmosphere, but is also the primary component in the atmospheric system (Kiehl and Trenberth, 1997). The ability to accurately measure its horizontal and vertical distribution is essential in such vital areas as numerical weather forecasting and climate studies, but is also applied in areas such as hydrometeorology and cloud microphysics. In regards to climate, water vapor monitoring is a key constituent in the global energy budget. It is also essential for constructing re-analysis data, as well as for long-term drought and flood risk assessment. Forecasters use water vapor data to initialize forecasting models, to determine horizontal and vertical atmospheric motion along with vorticity, and to diagnose red-flag and flash flood warning potential. Water vapor gradients are also studied because they are often initiation zones for both cyclogenesis and severe storms.

The global distribution of water vapor is a challenge to determine and can change rapidly in both space and time. Figure 1.1 shows a monthly average of total column water vapor taken from the NASA Water Vapor Project, known as NVAP.

As can be seen, water vapor has a very irregular pattern along with very strong gradients. The NVAP dataset is dependent on accurate measurements of water vapor that are amalgamated in order to put together global pictures such as in Figure 1.1.

Water vapor enters the atmospheric system in a variety of ways. It is most often introduced into the atmospheric system by evaporation from soil and land surfaces, rivers, lakes, and the oceans. Evaporation from the ocean surface accounts for up to 85% of the source of water vapor in the atmosphere (Jacobsen, 1999). Sublimation from glaciers and ice sheets, and transpiration from vegetation are also important sources for atmospheric water vapor. Water vapor is removed from the atmosphere through condensation, ice deposition, precipitation, as well as by gas-phase chemical reactions. The water vapor mixing ratio varies greatly with location, going from nearly zero at the poles to values of 4% water vapor per volume of air in the tropical regions (Jacobsen, 1999). The low mixing ratio values at the poles occur because at low temperatures, water vapor condenses and deposits as ice quite readily. Conversely, in the tropical regions water evaporates quite readily due to the warm surface temperatures. Water vapor density typically decreases exponentially with height, however its distribution is strongly affected by geographical location, the ambient atmospheric activity, the season, as well as the time of day.

The global energy budget is greatly affected by the presence of water vapor in the atmosphere. Water releases and absorbs large amounts of energy during phase changes. This results in energy exchanges with the surrounding air that affect the

vertical stability of the atmosphere, which can ultimately lead to clouds and precipitation. Latent heat release accounts for an exchange of 78 Watts per square meter in annual Earth global mean energy budget calculations (Kiehl and Trenberth, 1997). Water vapor also absorbs, emits, and scatters incoming solar radiation, as well as outgoing terrestrial radiation. These attenuation effects drive a significant portion of the radiation budget of the planet, contributing up to 60% of the total radiative forcing in clear sky (Kiehl and Trenberth, 1997).

Not only is water vapor a fundamental variable in the planetary radiation budget, but is also highly valuable in quantitative precipitation forecasting. Limitations in the analysis of water vapor are the major source of error in short-term (0-24 hours) precipitation forecasts (Bevis et al., 1992).

Several ground and space based methods are currently employed to determine its spatial and temporal variability. Such methods include the use of radiosondes, satellite-borne infrared sounders, Global Positioning System (GPS) measurements from both space based and ground based receivers, and microwave radiometers. Ground observation networks consist of approximately 1000 radiosondes and several thousand GPS stations globally. This leaves for large gaps in data, making satellites an attractive addition of knowledge. Along with poor resolution, radiosondes typically do not measure upper tropospheric water vapor well. Radiosondes are typically launched twice daily, giving them very poor time resolution as well. While the global GPS network has better spatial and time resolution than the radiosonde network, GPS measurements lack any meaningful profiling knowledge. GPS data does not thus far contain vertical knowledge of

water vapor distribution, and only provides total column estimates. Due to the sparse nature of these ground based observing stations, space-based radiometers have an advantage in sensing water vapor on a global scale. Satellite constellations can be used together to get observations over the entire globe daily.

Water vapor has shown to be one of the most important constituents in the atmospheric system, however, its temporal and spatial variability has been poorly measured on a global scale. Satellites have the unique opportunity of gathering large quantities of measurements over remote land and ocean regions worldwide, making them a needed resource for water vapor modeling.

1.2 Microwave Remote Sensing

Remote sensing is defined as the science and art of acquiring information about an object or an area through the analysis of data that is obtained by a device which is not in any type of contact with the object or area being sensed. The acquired data can take on many forms, such as acoustic wave distributions, force distribution variations, and electromagnetic energy distributions. The airborne and spaceborne sensors used in atmospheric science related remote sensing involve measuring the electromagnetic energy distributions. These types of sensors receive data on the emission and attenuation of electromagnetic energy as it passes through the atmosphere.

Satellite retrievals have been a major breakthrough in atmospheric science in the latter half of the 20^{th} century. Retrievals of atmospheric temperature and moisture

profiles, along with cloud tracking and various other parameters have greatly aided the progress of forecasting. Data is now used in data assimilation schemes that are used by forecasting models worldwide.

Several types of satellite remote sensing products are used. These products are typically broken down by the portion of the electromagnetic spectrum from which they receive radiant energy. Visible, infrared, and microwave radiation are the three portions of the spectrum that are typically used for atmospheric and surface remote sensing. Visible products can only be used during daylight hours due to their dependence on solar radiation, leaving large data gaps. Visible and infrared products can only see radiation emitted or scattered by the tops of the clouds, whereas radiation at microwave wavelengths can penetrate cloud layers. Microwave instruments have the unique advantage of being able to detect radiation from the atmosphere even in the presence of clouds, making them a more attractive candidate for retrieving global water vapor profiles.

Microwave remote sensing techniques were first developed and used in the 1930's as a means to measure energy from non-Earth sources. Microwave radiometers were used to measure emission from planets, stars, and other objects that lie within our galaxy and beyond. Only over the last thirty years has the focus changed from astrophysics to measuring atmospheric radiation emanating from our own planet.

Satellites are able to remotely measure radiation emanating from Earth's surface, from which we can estimate a variety of different atmospheric parameters including skin temperature, surface temperature, water vapor profiles, precipitation,

cloud liquid water, sea surface winds, ice and snow cover, soil moisture, and aerosol concentrations. The advantage of using the microwave spectrum for remote sensing of the atmosphere is its ability to penetrate through clouds at certain frequency ranges.

The microwave radiometer is a passive instrument, meaning that the radiometer is measuring transmission directly from the target source. This means that the signal is coming directly from the atmosphere and the Earth's surface. The antenna collects all radiation that has been emitted and scattered by the scene. The power that is emitted by the scene and received by the antenna is a function of the scene temperature; power and temperature are directly proportional in the microwave spectrum. For any given value of temperature, the maximum power that any scene can emit is equal to the power that would be emitted from a perfect blackbody. For perfectly emitting blackbodies, the power P can be described as:

$$P = k\varepsilon TB \quad (1.1)$$

where k is Boltzmann's constant, T is the temperature of the blackbody, ε is the background emissivity (assumed to equal 1 for a blackbody), and B is the bandwidth of the radiometer (Ulaby et al., 1981). The bandwidth is assumed to be narrow enough such that the spectral brightness can be assumed to be constant over the antenna pattern solid angle. The temperature in Equation 1.1 can be related to the radiometric brightness temperature by $T = {T_B}/{\varepsilon}$, and is used to describe the emission from a material using the following relation:

$$T_B = \frac{P}{kB} \quad (1.2)$$

where P now represents the power emitted by an object over a bandwidth B. These brightness temperature observations are very powerful, as they can be inverted using the principles of radiative transfer theory to accurately estimate atmospheric parameters such as water vapor and surface temperature (Ulaby et al., 1981).

There is no universally set definition of the microwave spectrum, but it is typically defined as either the region from 0.3 to 300 GHz in the electromagnetic spectrum, or radiation having a wavelength from 1 millimeter to 1 meter (Ulaby et al., 1981). The microwave transmission as a function of frequency can be seen in Figure 1.2. In the 1-15 GHz frequency range, the atmosphere appears transparent even in the presence of clouds and precipitation. This allows the radiometer to sense land and ocean surfaces in practically all meteorological conditions. These are better known as atmospheric window regions. Other frequencies are also used that are within the atmospheric window region, such as 35 GHz, to remotely sense Earth's surface. Oxygen absorption features lie in the 50-70 GHz region, as well as at 118.7 GHz. These oxygen absorption features are useful for remotely sensing the higher atmospheric layers, spanning from the tropopause up past the stratosphere. Water vapor absorption features can be found at 22.2 GHz and at 183.3 GHz. These water vapor absorption features are used in order to retrieve vertical profiles of both temperature and mixing ratio. The region between 89 GHz and the absorption band at 183.3 GHz is called the water vapor continuum. This portion of the spectrum has slightly increasing absorption from water vapor as the frequency approaches the 183 GHz absorption line. However due to the fact that absorption in this range is weak, this region allows radiometers to sense water vapor near or at the

surface. This is a huge advantage due to that fact that most of the atmospheric water vapor resides within the first kilometer of the atmosphere.

Microwave satellite sensors have been used to retrieve atmospheric state parameters for several decades, however the retrievals of certain parameters have not been performed satisfactorily over land thus far. Further discussion of the nature of this problem will be discussed in Chapter 2. Several methods have been and are being developed in order to overcome this problem. One such method will be presented in the scope of this research.

1.3 Scientific Objectives

Space-borne microwave radiometers capture radiation emitted from land and ocean surfaces that is passed through the Earth's atmosphere. The desired atmospheric parameters that are to be retrieved are determined using atmospheric transmission and radiative transfer functions (See Chapter 2). In order to accurately estimate the atmospheric transmittance, the surface emission must be known. Over the global oceans, the surface emission is well approximated within each viewing scene of the radiometer. The oceans are homogenous on small scales, and the sea surface temperatures, salinity, and surface wind speeds can be easily measured.

Over land, however, microwave radiometers have a much harder time accurately retrieving parameters such as temperature and water vapor due to the nature of the background emissivity. Retrievals rely on the ability to extract the atmospheric state from the upwelling radiation, most of which comes from emission

from the surface. Knowing the surface emissivity to a high degree of accuracy is essential for calculating the land surface temperature, however it is also important because this emission must be removed in order to retrieve the atmospheric parameters desired (Jones et al., 2004). Land type, vegetation, snow, ice, rain, urbanization effects, and many other factors have an effect on the aggregate emission within each viewing scene. This results in a strong sensitivity and variability of microwave emissivity on small scales. Accurately modeling these emissivity gradients becomes nearly impossible considering that the typical microwave satellite footprint ranges anywhere from 10 to 50 km.

Along with the problem of high spatial variability comes the problem of high temporal variability. Vegetation, snow, and ice have a seasonal cycle, and precipitation has a strong effect over short time scales. Due to this lack of homogeneity in time and space, retrievals over land can become quite cumbersome.

Several methods are currently being developed in order to extract atmospheric state parameters despite this background emission difficulty. A physically based iterative optimal estimation retrieval has been implemented to retrieve atmospheric parameters from a microwave satellite platform, and was the focus of this research. This retrieval is based on the method of Engelen and Stephens (1999). The retrieval uses a first guess of water vapor and temperature profiles, and uses a first guess of emissivity at each of five frequencies. The retrieval is further discussed in Chapter 4.

The land surface emissivity problem will be discussed in further detail in Chapter 2, along with a quick review of radiation and radiative transfer with respect

to the microwave spectrum. The majority of energy present in the atmospheric system comes from solar electromagnetic radiation. Part of this energy is scattered and absorbed by particles in the atmosphere, while the rest is transmitted to the surface. Absorption and emission of radiation causes an exchange between thermal energy and electromagnetic energy. These processes are explained and handled using radiative transfer theory and the radiative transfer equation.

The microwave satellite platform data being used in the retrieval will come from the Advanced Microwave Sounding Unit (AMSU). AMSU is a 20-channel microwave radiometer with 15 channels for temperature sensing and 5 channels for water vapor sensing. A bias removal method was developed for the Advanced Microwave Sounding Unit-B (AMSU-B), which consists of channels 16-20, in order to remove side-lobe contamination (see Section 3.2). Such a procedure had not been previously implemented, and its effect on the retrieval will be briefly discussed.

The 1DVAR retrieval was run over land and was validated against Global Positioning System (GPS) and radiosonde measurements in order to isolate bias in the retrieval. Background information on GPS and radiosondes can be found in Chapter 3.

Within the retrieval lies the Jacobian, which defines the sensitivity of the forward model to perturbations in the atmospheric state vector. These sensitivities are able to determine if enough sensitivity exists at certain frequencies to produce a noticeable atmospheric signal. They also give us an expectation of how well we

can retrieve particular parameters under certain background conditions. Sensitivities are plotted and presented in Chapter 5.

The preliminary "best case" results of the optimal estimation retrieval of water vapor over land will be discussed and validated against similar measurements from the GPS and radiosonde networks. These results are presented in Chapter 6. Future work and improvements are also discussed.

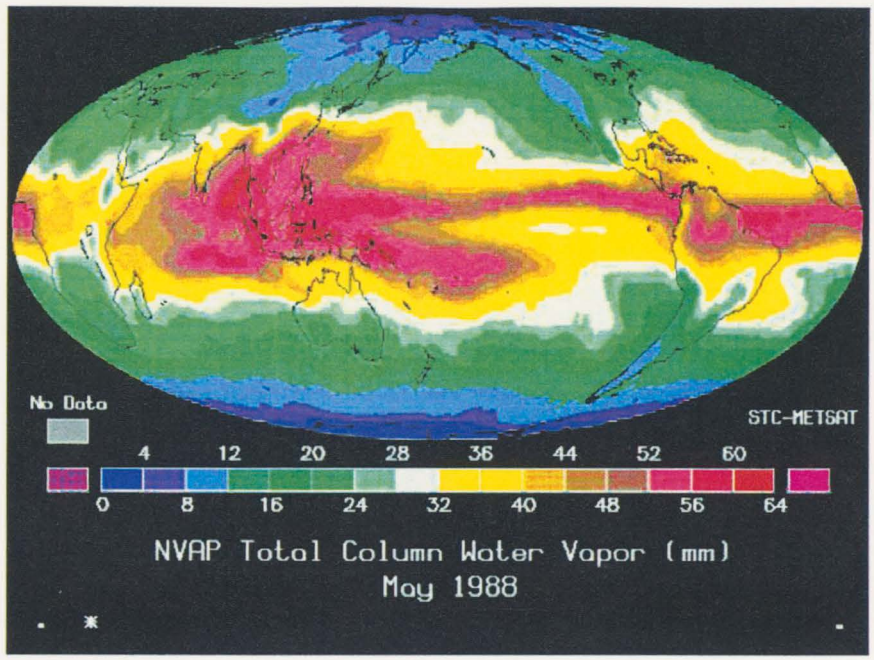

Figure 1.1: Monthly averaged column water vapor values from NVAP. As can be seen, water vapor is highly variable, even over monthly averages.

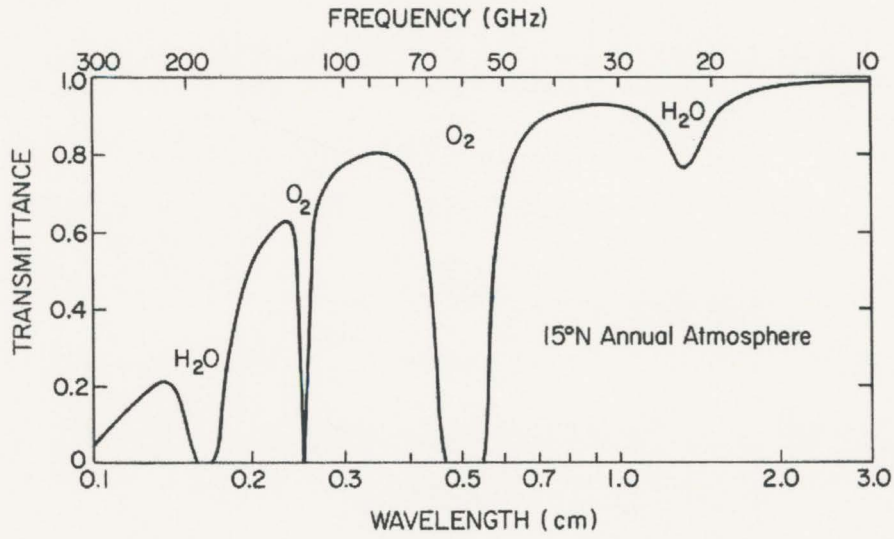

Figure 1.2: Transmittance in the microwave spectrum. There are two oxygen absorption features (near 60 and 118 GHz) and two water vapor absorption features (near 22 and 183 GHz).

CHAPTER 2: MICROWAVE REMOTE SENSING OVER LAND

2.1 Radiative Transfer

Satellites do not measure any quantity directly except for the radiance emanating from the viewing scene. Models are used in order to extrapolate the atmospheric parameters desired from these radiances. In order to create such a model, the physics of radiation and knowledge about its travel through the atmosphere must be characterized properly. Without considering polarization effects, the propagation of radiation along a straight path, *s*, can be affected by four processes: radiation can be absorbed by a medium, emitted by a medium, scattered by a medium, and radiation from other sources can be scattered into the path. The radiation that is detected by the radiometer is a combination of both surface emission and scattered solar radiation. The amount of surface radiation reaching a satellite is described by the transmission function. The following sections provide a roadmap for the information needed in order to obtain a clear picture of the physics of space remote sensing.

2.2 Transmittance

The transmittance of radiation through the atmosphere is the fraction of emitted power to the received power, which is represented by a number between 0 and 1

with 0 being a completely opaque atmosphere, and 1 being a completely non-attenuating atmosphere. The transmittance function for the atmosphere is given by:

$$\tau_\nu(s_1, s_2) = \frac{L_\nu(s_1)}{L_\nu(s_2)} = e^{-\delta(s_1, s_2)} \qquad (2.1)$$

where $L_\upsilon(s_i)$ is the radiance at point s_i.

The radiative transfer equation can be further simplified by incorporating the plane-parallel approximation. The optical path through a horizontally homogeneous atmosphere is approximated by $\sec\theta \cdot dz$ where θ is the zenith angle and dz is the normal optical path length. This results in a new expression for the transmittance:

$$\tau_\nu(\theta, p_1, p_2) \approx e^{-\sec(\theta)\delta(p_1, p_2)} \qquad (2.2)$$

where p_1 and p_2 are pressure levels.

A rapid radiative transfer model for the Advanced Microwave Sounding Unit (AMSU) was developed using a rapid transmittance algorithm for non-precipitating conditions (Deeter and Evans, 1998). The algorithm uses a polynomial approximation to the temperature dependence of oxygen-band opacity within atmospheric layers (Deeter and Evans, 1998). Lookup tables were created in order to calculate the local water-vapor line intensity and pressure-broadening parameters, as well as the contributions to absorption from the water-vapor continuum and other sources.

For a given atmospheric layer, the channel-average transmittance is given by:

$$\langle \tau(P_1, P_2) \rangle = \exp\{-(\alpha + \beta V + \gamma L)\} \qquad (2.3)$$

where P_1 and P_2 are the pressures at the boundaries, α is the opacity of fixed gasses in the layer, V is the vertical column density integral of water vapor between the two pressure levels, and L is the cloud liquid vertical column density integral. The coefficients α, β, and γ are pre-computed for each layer given temperature, pressure, V, and the secant of the observation angle from retrieval algorithm.

2.3 Thermal Emission

The amount of radiation emitted from a source is defined as its thermal emission. The intensity of blackbody radiation emitted by a source as a function of wavelength is given by the Planck Function:

$$\beta_\lambda(T) = \frac{2hc^2\lambda^{-5}}{\exp\left(\frac{hc}{\lambda k_B T}\right)-1} \qquad (2.4)$$

where h is Planck's Constant, c is the speed of light, and k_B is the Boltzmann Constant. As can be seen in Figure 2.1, the Planck function is non-linear in temperature. In the microwave spectrum, temperatures that are typically observed over earth lie in the high temperature asymptote region of this function. This allows brightness temperatures to be substituted into the radiative transfer equation in place of radiance with accuracy on the order of hundredths of a Kelvin. This is known as the Rayleigh-Jeans approximation, and is valid for radiation of the longer wavelengths.

No source emits as a perfect blackbody due to simple conservation laws. Because of this, the spectral emissivity (ε_λ) is used as a measure of the ratio of emitted radiation to that emitted as if that source were a perfect blackbody at a designated wavelength. This results in a value between zero and one, with zero meaning no emission, and one representing a pure blackbody emitter. The emissivity is directly proportional to the final emanating radiation at a particular wavelength (L_λ) by the following relation:

$$L_\lambda = \varepsilon_\lambda \beta_\lambda(T) \qquad (2.5)$$

Emissivity has a strong wavelength dependence and is also dependent upon viewing angle and the temperature of the viewing scene. The dependence on view angle is a function of the azimuth and zenith angle. The temperature dependence is small and typically negligible at terrestrial temperatures.

The radiative transfer equation for a plane-parallel microwave radiative transfer regime can be rewritten in a more straightforward fashion using the surface emissivity. This form of the equation has a surface emission term, an atmospheric emission term, and an emission term corresponding to downward atmospheric emission that is reflected and retransmitted from the surface back through the atmosphere:

$$T_B = \varepsilon T_s e^{-\tau_A} + (1-\varepsilon) e^{-\tau_A} T_D + T_U \qquad (2.6)$$

where T_B is the brightness temperature, ε is the emissivity, T_S is the surface temperature, $e^{-\tau_A}$ is the atmospheric transmission, (1-ε) is the reflectivity of the surface, T_D is the downwelling atmospheric radiation emanating from the atmosphere, and T_U is the upwelling atmospheric emission (Ruston, 2004). Note

that the atmosphere is assumed to be non-scattering in this equation because it assumes a cloud-free atmosphere. In order to keep consistent with the laws of conservation, the transmissivity, emissivity, and reflectivity of the surface must be equal to one.

2.4 Atmospheric Absorption

Molecular absorption of radiation occurs when a molecule transitions from a lower to a higher energy state. These transitions can involve combinations of changes in electrical, vibrational, and rotational energies.

The absorption spectrum that is caused by any single transition is referred to as an absorption line. Groups of these lines can be found together, and are often referred to as a band. An example of a banding feature is shown by comparing the rotational and vibrational transition modes of a molecule. Rotational energy changes require a significantly lower amount of energy than vibrational changes. Small amounts of energy can be introduced into the system that can facilitate the rotational transitions without being enough to fuel a vibrational transition, resulting in rotation lines. However when enough energy is given to the system to force a vibrational transition, several rotational transitions are also forced. This gives rise to the series of lines known as the rotation-vibration band. When simultaneous changes of all three mentioned energy states occur, complex band systems result due to the large energy differences that are associated with the electronic transitions.

Oxygen and water vapor have the strongest absorption bands in the microwave spectrum compared to other gases readily found in the earth's atmosphere. Due to the permanent magnetic moment of oxygen, magnetic interaction with the incident field creates rotation lines centered near 60 GHz, as well as a single line at 118 GHz. Water vapor has an electric dipole, producing rotation lines around 22 GHz, 183 GHz, and in the far-infrared region. Figure 1.2 shows the transmission of microwave radiation as a function of frequency.

2.5 Surface Effects-Emissivity Impacts

Atmospheric parameters are remotely sensed by measuring transmission of radiation at varying wavelengths as it passes through the earth's atmosphere en route to the space-borne radiometer. In order to isolate the atmospheric transmission functions, the surface emission must be removed from the detected radiance.

Characterizing the surface emission is a very involved and complex process. The emission can change rapidly on small scales over land due to a large number of effects. The electromagnetic properties of the land surface constitute some of these effects. Soil moisture content has a profound effect on the surface emittance, and can lead to surface emissivities ranging from nearly 1 for dry soil, to an emissivity of 0.6 or less for wet soils. The surface emittance of water is typically around 0.5, producing a very cold surface thermal emission. This leads to the clouds having a warmer emission signature when compared to the cold background over ocean

surfaces, because clouds emit microwave radiation much more efficiently at higher brightness temperatures. Due to these effects, clouds and atmospheric water vapor can be easily detected because brightness temperature differences can be easily measured. This technique does not work over land, however, because land surfaces typically have much higher thermal emission.

Other surface features influence the surface emittance, such as surface roughness and inhomogeneities. Over ocean surfaces, these are typically caused by wind and salinity differences. Vegetation changes, topography, and soil types can all be factors over land. As these effects become greater, the surface scattering has a much larger diffuse component.

With all of these surface influences in mind, it is easy to see how cumbersome it is to attempt to model these changes on large scales. Many satellite retrieval methods depend on these models in order to formulate a first guess of the background emissivity in a retrieval.

2.6 New Methods for a First Guess of Emissivity: The Microwave Emissivity Model (MEM)

Due to the highly variable nature of the background emissivity, new methods have been produced in order to quantify land emissivity under a variety of surface conditions. A microwave land emissivity model (MEM) was created at NESDIS to be directly implemented into numerical prediction models and is used as a first

guess in the 1-dimensional variational retrieval (1DVAR) used in this research. Figure 2.2 shows an example emissivity map from the MEM.

The MEM was developed by simulating and measuring the microwave emissivity spectra over a range of surface conditions at different frequencies. Bare soil emissivities were modeled only at lower frequencies where they could be empirically adjusted by ground measurements and are a function of surface roughness, soil type, and soil moisture. The emissivity of vegetation-covered regions was simulated using a simplified radiative transfer model with optical parameters derived using the Rayleigh approximation. Optical parameters over snow-covered surfaces were developed using an effective wave propagation constant for the incident medium.

The surface in the MEM is represented as a three-layer medium above an irregular subsurface. The upper and lower levels are defined as spatially homogeneous with uniform dielectric constants. The middle level contains inhomogeneous scattering elements, such as snow, sand, and vegetation. The reflectances at the two interfaces are determined using modified Fresnel equations, and the volumetric scattering for this layer is determined by manipulating the following radiative transfer equation:

$$\mu \frac{dI(\tau,\mu)}{d\tau} = I(\tau,\mu) - \frac{\omega(\tau)}{2}\int_{-1}^{1} P_s(\tau,\mu,\mu')I(\tau,\mu')d\mu' - [1-\omega(\tau)]B(T) \tag{2.7}$$

where I is the radiance, μ is the cosine of the zenith angle, μ' is the cosine of the scattering zenith angle, $\omega(\tau)$ is the single-scatter albedo, P_s is the phase function, and $B(T)$ is the Planck function evaluated at thermal temperature T (Weng et al.,

2001). The solution for arbitrary viewing angles is described using a two-stream approximation given by:

$$\mu \frac{dI(\tau,\mu)}{d\tau} = [1-\omega(1-b)]I(\tau,\mu) - \omega b I(\tau,-\mu) - (1-\omega)B \qquad (2.8)$$

and

$$\mu \frac{dI(\tau,-\mu)}{d\tau} = [1-\omega(1-b)]I(\tau,-\mu) - \omega b I(\tau,\mu) - (1-\omega)B \qquad (2.9)$$

where b and 1-b are the ratios of the integrated scattering energy in the backward and forward directions (Weng et al., 2001).

It is assumed that ω, b, and B are independent of τ, which allows equations 2.8 and 2.9 to be combined into two decoupled second-order differential equations with constant coefficients. Once the equations are of this form, they can be used to analyze the atmospheric and surface scattering. The formulation of the optic parameters for vegetation and other surface features can be found in Weng et al., 2001, and will not be further discussed here.

Efforts are being taken to further improve the MEM. Vertical stratification for snow-covered surfaces, increasing the number of surface types for the optical parameter calculations, and adding radiative transfer streams for crop stems and tree trunks will aid in the improvement of this already sophisticated model for future applications.

2.7 The Radiative Transfer Equation

All of the parts needed to describe the travel of electromagnetic radiation through the atmosphere have been introduced, and may now be put together in order to form the Radiative Transfer Equation (RTE). The attenuation and propagation of electromagnetic radiation through the atmosphere can be described through the use of the RTE, which in its general form is written as

$$\frac{dL_\nu(r,\Omega_s)}{ds} = \sigma_e\left[J(r,\Omega_s) - L_\nu(r,\Omega_s)\right] \qquad (2.10)$$

where $L_\nu(r,\Omega_s)$ is the spectral radiance at a frequency ν at a location r in direction Ω_s, σ_e is the atmospheric extinction coefficient, and $J(r,\Omega_s)$ is the total source function at r in the direction Ω_s (Chandrasekar, 1960). The atmospheric extinction coefficient contains the sum of the absorption and scattering effects on radiation passing through the atmosphere. The two terms on the right side of Equation 2.10 describe this extinction, as well as characterizing the thermal emission and scattered radiation that is introduced into the beam.

In order for a satellite to calculate Earth radiances, the radiative transfer equation must be integrated over the entire depth of the atmosphere. To do this, the concept of optical thickness, δ, which serves as the integrated optical depth between two points, is introduced:

$$\delta(s_1,s_2) = \int_{s_1}^{s_2} \sigma_e ds \qquad (2.11)$$

where s is the path between the points s_1 and s_2. The formal solution to the radiative transfer equation integrated along a path s can be obtained by multiplying Equation 2.10 by $e^{\delta(c,s')}$ to yield (Chandrasekar, 1960):

$$L_\nu(s) = L(0)e^{-\delta(0,s)} + \int_0^s \sigma_e(s')J(s')e^{-\delta(s',s)}ds' \qquad (2.12)$$

with $s = 0$ being the surface boundary. The total source function can now be expressed, including all attenuation effects, as:

$$J(r,\Omega_s) = (1-\tilde{\omega})B_\nu[T(r)] + \frac{\tilde{\omega}}{4\pi}\int_0^{4\pi}\xi(r,\Omega_i,\Omega_s)L_\nu(r,\Omega_i)d\Omega_i \qquad (2.13)$$

where $B_\nu(T)$ is the Planck function for a temperature T, and $\tilde{\omega}$ is the single scatter albedo given by:

$$\tilde{\omega} = \frac{\sigma_s}{\sigma_a + \sigma_s} \qquad (2.14)$$

and $\xi(r,\Omega_i,\Omega_s)$ is the scattering phase function. The single scatter albedo is used to determine whether scattering or absorption is dominant, based on its magnitude. The scattering phase function gives the probability that incident energy from direction Ω_i at position r is scattered into direction Ω_s.

For retrievals from the Advanced Microwave Sounding Unit (AMSU), a simplified version of the radiative transfer model is used in order to calculate a brightness temperature. The equation of radiative transfer is given by:

$$T_B = T_{direct} + \tau\left[T_{bs} + T_{sky}\left(1 - \frac{T_{bs}}{T_s}\right)\right] \qquad (2.15)$$

where T_B is the brightness temperature emitted at the top of the atmosphere, τ is the atmospheric transmittance, T_{direct} is the atmospheric brightness temperature component on a direct path to space, T_{bs} is the surface brightness temperature, T_s is the surface temperature, and T_{sky} is the sky brightness temperature as observed from

the surface (Rosenkranz, 2001). The advantage of using this form of the equation allows for the separation of the calculation of surface brightness from the calculation of temperature. It is essentially the same equation as 2.10. The radiance detected by the satellite at height, s, is described by the brightness temperature in the microwave region, T_B. The first term describes the component of the surface emission that is on a direct path to the radiometer. The last, and more complicated term, describes the transmission of radiation along a path using simple radiances as opposed to the source function used in Equation 2.10.

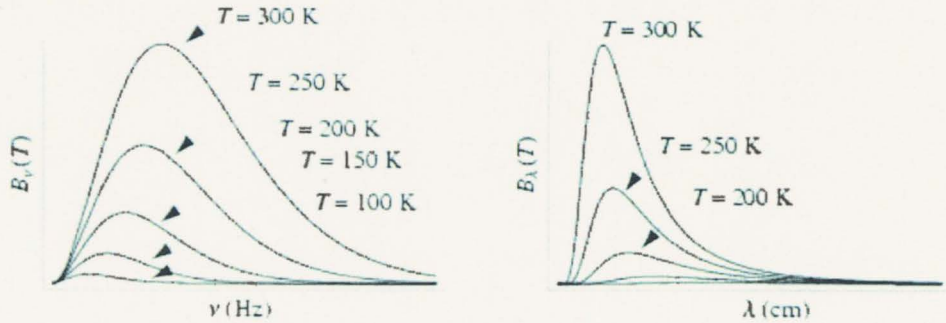

Figure 2.1: Examples of the structure of the Planck Function, both as a function of frequency and wavelength.

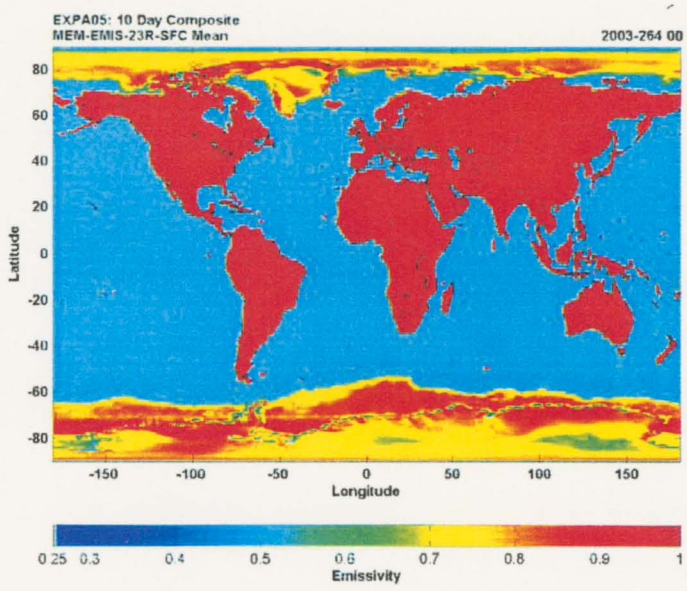

Figure 2.2: An example image of global emissivity from the Microwave Emissivity Model (MEM). Courtesy of A. Jones, CIRA.

CHAPTER 3: DATA SOURCES AND SPECIAL PROCESSING

3.1 The Advanced Microwave Sounding Unit-B

The Advanced Microwave Sounding Unit-B (AMSU-B) is a 5-channel microwave radiometer that receives and measures radiation emanating from various layers in the atmosphere in order to provide global humidity profiles. Currently AMSU-B is operating aboard the NOAA Polar Orbiting Environmental Satellites 15, 16, and 17. AMSU-B is also capable of identifying precipitation, as well as snow and ice cover. When used with the Advanced Microwave Sounding Unit-A (AMSU-A), these two instruments allow global soundings of humidity, temperature, and cloud liquid water path. Together, AMSU-A and AMSU-B comprise a 20-channel microwave radiometer, with AMSU-B covering channels 16-20 (see Figure 3.1).

The five channels of AMSU-B are divided into five frequencies: 89 GHz, 150 GHz, 183.31 +/- 1 GHz, 183.3 +/- 3 GHz, and 183.3 +/- 7 GHz. The 89 and 150 GHz channels (Channels 16 and 17 respectively) have relatively low atmospheric absorption and are only marginally affected by the water vapor and oxygen absorption line wings. These channels are better suited to measure water vapor that is near the surface. Channels 18, 19, and 20 reside in a strongly opaque water vapor absorption band and therefore are unable to penetrate as deep into the atmosphere as Channels 16 and 17.

Brightness temperature sensitivities for AMSU generally lie around 0.5 K, but can span up to about 1.0 K (Saunders et al., 1995). These sensitivities, also known as noise equivalent temperatures, are a measure of the minimum change in antenna temperature detectable by the receiver.

AMSU-B is a cross-track scanning instrument with a field of view (FOV) of 1.1° +/- 10% and measures 90 earth views, plus four space views and four internal blackbody target views, every 8/3 seconds. The AMSU-B instrument uses a scanning parabolic reflector antenna that focuses radiation into a quasi-optic system that separates the frequencies into three separate feed horns.

Earth view radiances are computed from measured counts using calibration coefficients derived from the internal blackbody and space view calibration source data. The physical temperatures of the internal blackbody calibration targets are measured with the use of Platinum Resistance Thermometers, otherwise known as PRT's. The output from the PRT is in counts, so this number must be converted to a PRT temperature. The NOAA KLM satellites (NOAA 15, 16, and 17) are designed to derive PRT temperatures from counts in a single step process using the following polynomial relation:

$$T_k = \sum_{j=0}^{3} f_{jk} C_k^j \qquad (3.1)$$

where T_k is the temperature and C_k is the count of the PRT, and f_{kj} are coefficients that are provided for each of the PRT's (Goodrum et al., 1999). The mean blackbody temperature is then calculated by computing a weighted average of all of the PRT temperatures as shown in Equation 3.2:

$$T_w = \frac{\sum_{k=1}^{m} w_k T_k}{\sum_{k=1}^{m} w_k} + \Delta T_w \qquad (3.2)$$

where m is the number of PRT's (m=7 for AMSU-B), w_k is the assigned weight for each PRT, and T_w is the warm load correction factor for each channel (Goodrum et al., 1999). There also exists a cold space correction given by ΔT_c which describes the contamination of the space view by radiation from the satellite platform. The corrected cold space temperature is expressed by the following relation:

$$T_c = 2.73K + \Delta T_c \qquad (3.3)$$

where 2.73 K is the cosmic background temperature. The ΔT_c term is provided by post-launch analysis and represents the antenna side lobe interference with the satellite platform.

Further calibration must take place to convert observed counts into radiances due to nonlinear contributions arising from the use of imperfect square law detectors. Equation 3.4 calculates the scene radiance, R_s, as follows:

$$R_s = R_w + \frac{C_s - \overline{C}_w}{G} + Q \qquad (3.4)$$

where R_w and R_c are Planck radiances corresponding to T_w and T_c respectively, C_s is the radiometric count from the Earth scene, $\overline{C}_w$ and $\overline{C}_c$ are the averaged blackbody and space view counts, G is the channel gain, and Q is the quadratic contribution term (Goodrum et al., 1999). The channel gain, G, is given by:

$$G = \frac{\overline{C}_w - \overline{C}_c}{R_w - R_c} \qquad (3.5)$$

The quadratic contribution term, Q, is given by:

$$Q = u\frac{(C_s - \overline{C}_w)(C_s - \overline{C}_c)}{G^2} \qquad (3.6)$$

where u is a predetermined parameter that is provided for three principal instrument temperatures, and can be determined for all temperatures by interpolating between the these three principle values (Goodrum et al., 1999).

The monochromatic assumption breaks down for Channels 19 and 20 due to the fact that these channels span as much as 14 GHz, therefore a band correction must be applied. Two coefficients (b and c) are introduced in order to produce a more accurate blackbody temperature (Goodrum et al., 1999):

$$T'_w = b + cT_w \qquad (3.7)$$

3.2 Antenna Pattern Correction for AMSU-B

The microwave radiometer on AMSU-B receives around 95% of the total power from the antenna's mainbeam, which is typically pointed at an Earth scene. The remaining 5% or so of the energy comes from Earth, cold space, and satellite platform, which introduces a bias into the mainbeam brightness temperature. Figure 3.1 gives the exact main beam and wide beam efficiencies for Channels 16-20. Removing these sidelobes is essential to eliminate a bias in the retrieved brightness temperature. This procedure is known as an antenna pattern correction.

The original AMSU-B antenna pattern corrections (Hewison and Saunders, 1996) are available in the Advanced Television Infrared Observation Satellite (TIROS) Operational Vertical Sounder (ATOVS) and Advanced Very High

Resolution Radiometer (AVHRR) Processing Package (AAPP) under a non-distributable license from the European Organisation for the Exploration of Meteorological Satellites (EUMETSAT). This work was carried out in order to provide a publicly available AMSU-B antenna pattern correction, as well as to show its impact on physical temperature and water vapor retrievals.

The antenna pattern correction for AMSU-B was developed using both main beam and wide beam antenna efficiencies for channels 16-20 along with the corresponding solid-angle viewing regions to determine the radiometric gain emanating from the earth (and the atmosphere below 20 km) as opposed to cold space. The results allow an improved estimate of AMSU-B brightness temperatures. The difference between the predicted radiance and the radiance for each channel in each viewing region gives a correction factor that must be included in the calculation of the viewing region radiance in order for the radiometric calibration to avoid a consistent bias in the radiometric gain. Using a simplified version of the antenna pattern and a set of atmospheric brightness temperatures, antenna pattern corrections were simulated for each channel. An example of a ground calibrated antenna pattern with sidelobes is shown in Figure 3.2.

Two related approaches are summarized in Nielsen et al., 2005. The satellite platform has been shown to have a negligible effect on the energy received by the antenna system (Mo, 1999), therefore it is not addressed in this procedure. The ground based antenna pattern is also not used in this development as it was in earlier methods due to the fact that the antenna pattern changes once the radiometer

is space borne. Therefore a simple top-hat approximation to the gain function is made. The cosmic background temperature is assumed to be 2.73 K.

In order to separate the radiation coming from the earth from the cold space sidelobes, an earth fraction must be calculated to quantify how much of the satellite viewing scene is occupied by the earth. The Earth Fraction, $F = \Omega_{Earth}/2\pi$, was computed for both a two-dimensional approximation and the true three-dimensional Earth (Nielsen et al., 2005). The unapproximated three-dimensional case was shown not to have significantly improved the accuracy of the corrections.

Nielsen et al., 2005, started by computing the Earth Fraction using a two-dimensional approximation where the Earth is seen as a disk from the satellite. Figure 3.3 shows the Earth disk as it lies under the true curvature of the Earth. It should be noted that the Earth disk is not located at the center of the Earth but rather at the point where the satellite views make a tangent to the sphere of the Earth.

The solid angle that the Earth subtends within a viewing scene is given by:

$$\Omega_{Earth} = \pi(1-\cos\alpha) + \left\{ \sin^{-1}\left(\frac{\sin\theta'}{\sin\alpha}\right) - \cos\alpha \sin^{-1}\left(\frac{\tan\theta'}{\tan\alpha}\right) \right\} \qquad (3.8)$$

where α is the maximum angle at which the Earth can be seen from the satellite position, and θ' is the angle of intersection of the satellite viewing scene with the edge of the Earth.

The antenna pattern corrections can now be defined as the difference between the actual observed brightness temperature and the retrieved antenna temperature, $\Delta T = T_B - T_A$. This work adopted the approach of Jet Propulsion Laboratory (2000) using the AMSU-B specific earth fractions and antenna efficiencies (see

Figure 3.1). A numerical algorithm is employed to analytically compute the earth fraction based on the two-dimensional approach, and incorporated with the JPL antenna pattern correction method.

Channel 16 had the strongest sidelobe contamination since its corresponding main beam efficiency is 94.4%, leaving 5.6% of the antenna power susceptible to the sidelobes. Corrections are shown for a temperature domain of 150-250 K and can be seen in Figure 3.4. Results range from 3.9 K to 7.5 K depending upon the scan angle and the scene brightness temperature. The Channel 16 fractional corrections ranged from 2.65% to 3.10%.

Channel 17 and 18 had a lower fractional bias, in the range from 2.3% to 2.7%. The smallest correction was found in Channels 19 and 20, which the highest corresponding main beam efficiency (96.9%). The fractional corrections for these channels were in the range from 1.45% to 1.7%.

In order to demonstrate how the AMSU-B APC will affect atmospheric retrievals, an experiment was performed with an atmospheric profiling retrieval that uses AMSU-A and AMSU-B measurements (McKague et al., 2001; 2003). The retrieval is an optimal estimation technique that simultaneously solves for surface temperature, surface emissivity and atmospheric water vapor and temperature profiles (Rodgers, 1976; Englen and Stephens, 1999). The Liebe and Hufford (1993) microwave propagation model is used for gaseous absorption. The retrieval iterates through the retrieved variables and compares the calculations of the forward radiative transfer model to the AMSU measurements. The retrieved atmosphere is

also compared to *a priori* statistics to calculate a cost function, which is then minimized.

A total of 516 retrievals were compared, throughout all AMSU viewing angles. The APC has greatest effect at higher viewing angles, as was shown in Figure 3.4. The retrieval dataset consists of match ups between NOAA-15 and coastal and island radiosonde sites from the year 2000. The result presented here is expected to be typical but not unique. In an optimal estimation retrieval, the weight given to the observations versus *a priori* expectations in the final solution can be adjusted, so there is no one single set of results which quantifies the impact of the APC in the retrieval.

Figure 3.5 shows the mean difference in retrieved variables with and without the AMSU-B APC. The Mo ,1999, AMSU-A APC was applied to AMSU-A antenna temperature data in both cases. The AMSU-B APC has an impact on the entire retrieval vector. The APC has the effect of increasing the surface temperature by 0.5 K. The surface emissivities are slightly lowered within the physical retrieval to compensate. The greatest effect of the APC is on the moisture retrievals. At 300 and 500 mb, the mixing ratio increased by over 10 % when the APC was applied. The AMSU-B 183 GHz channels peak in the upper troposphere, so they have enhanced sensitivity to upper tropospheric moisture. The positive increase of moisture with the APC applied (warmer brightness temperatures) is expected since the retrievals were performed over ocean. Atmospheric moisture warms the brightness temperatures above the radiometrically cold ocean surface. The APC has progressively less effect on the retrieved moisture below 500 mb, indicating that

the measurements are having a decreasing impact on the solution as the surface is approached. The temperature retrievals are warmed throughout the column, but only by a fraction of a percent. In order to simulate the warmer radiances when the APC is applied, the retrieval both adds moisture and slightly increases the temperature.

The AMSU-B APC can be considered a "fine tuning" of the radiances from that instrument. The impact on a representative retrieval shows that the APC has a tangible impact on atmospheric and surface property retrievals from satellite. Upper tropospheric moisture is of critical importance in controlling the radiative balance of Earth and is the subject of much scientific investigation. A properly applied AMSU-B APC will have a meaningful impact on retrieved tropospheric moisture values. This impact should be accounted for in studies where high retrieval fidelity is required, such as data assimilation and climate science.

Antenna pattern corrections are an essential part of passive microwave remote sensing data treatment. Removing errors and biases from data assures that information that is passed into data assimilation systems and forecast models is accurate and useful. Employing an antenna pattern correction will assure that far sidelobe contamination has been taken into account, thereby increasing the accuracy and confidence of temperature and water vapor observations globally. Long-term climate studies will benefit from the treatment of AMSU-B data presented here.

3.3 The Global Positioning System

The Global Positioning System (GPS) was originally developed by the Department of Defense in order to produce extremely accurate estimates of global position, as well as velocity and time. The current navigational system consists of 24 satellites flying in 6 orbital planes approximately 20,000 km above the surface of the Earth. The satellites transmit an L-band pseudo-random square wave signal at 1.575 and 1.228 GHz to ground based receivers (Rocken et al., 1993). GPS measurements have a distinct advantage in the remote sensing world, as measurements can be performed in all weather, are in continuous operation, have high temporal resolution, have extremely high accuracy, have long-term stability, and are a data set independent from radiosondes that can aid in establishing a climate record.

The GPS Observation Equation was created in order to calibrate measurements and remove biases that may exist on the sub-centimeter level. The equation is of the following form (Rothacher, 2004):

$$L_r^s = \rho_r^s + c\delta t_r + c\delta t_{r,sys} - c\delta t^s - c\delta t_{sys}^s + \delta\rho_{trp} + \delta\rho_{ion} + \delta\rho_{rel} + \delta\rho_{mul} + N_r^s + \ldots + \varepsilon \tag{3.9}$$

where:

- ρ_r^s = Geometrical distance between the satellite and receiver
- δt_r = Station clock correction
- $\delta t_{r,sys}$ = Delays in receiver and antenna (cables, electronics…)
- δt^s = Satellite clock correction

- $\delta t_{s,sys}$ = Delays in satellite (cables, electronics…)
- $\delta \rho_{trp}$ = Tropospheric delay (due to atmospheric parameters)
- $\delta \rho_{ion}$ = Ionospheric delay (due to atmospheric physics)
- $\delta \rho_{rel}$ = Relativistic corrections
- $\delta \rho_{mul}$ = Mutlipath, scattering, and bending effects
- N_r^s = Phase Ambiguity
- ε = Measurement error

In order to ensure the high accuracy of GPS measurements, the station position and station motion must be calculated with high efficiency. The station position in an Earth-fixed frame is given by:

$$r_{r,e}(t_r) = r_{r,0} + v_r(t_r + t_0) + \delta r_{r,sol} + \delta r_{r,pol} + \delta r_{r,ocn} + \delta r_{r,atm} + \delta r_{r,ant} \tag{3.10}$$

where $\delta r_{r,sol}, \delta r_{r,pol}$ are the solid Earth and pole tides, $\delta r_{r,ocn}, \delta r_{r,atm}$ are the atmospheric and ocean loading terms, $\delta r_{r,ant}$ is the antenna phase center offset and variation, and $r_{r,0}, v_r$ are the station coordinates and velocities (Rothacher, 2004). In order to estimate the tropospheric delay, which is what gives information on water vapor, all of these terms must be modeled on the sub-centimeter level. Plate rotations can be easily modeled as a rotation of a rigid plate with angular velocity ω. As can be seen from Figure 3.6, the plate motion is typically less than about 20 mm/year. The pole tides are caused by the reaction of the elastic Earth to the change of its rotation axis. This typically has an effect of about 3 cm on the station coordinates. The weight of the atmosphere, also known as the air pressure, can vary

station heights up to 2 cm as it presses down on the continental plates. A similar effect is caused by the weight of the oceans on the plates that changes during tides. This effect is typically on the order of a few centimeters, and is observed well inland, not just in coastal areas.

The satellite position is in an inertial reference frame is given by:

$$r_i^s(t^s) = r_{i,0}^s(t^s; a, e, i, \Omega, \omega, t_p; p_1, p_2, \ldots, p_d) + \delta r_{ant}^s(t^s) \qquad (3.11)$$

where $r_{i,0}^s, \delta r_{ant}^s$ is the center of mass position and antenna phase center offset, $a, e, i, \Omega, \omega, t_p$ are the orbital elements, and $p_1, p_2, \ldots, p_d$ are the dynamical parameters (gravity field coefficients, air drag and radiation pressure parameters and so forth) (Rothacher, 2004). The high-precision satellite positions are computed by numerical integration by the International GPS Service.

The desired atmospheric parameters that are retrieved from GPS measurements are imbedded within the tropospheric delay term ($\delta\rho_{trp}$). As the GPS signal propagates between the satellite and the Earth-based receiver, it becomes refracted and delayed in the ionosphere and the neutral atmosphere. If all of the other delay terms in the observation equation are accurately calculated, then the atmospheric delay can be extracted. From this delay, the Total Precipitable Water (TPW) can be determined.

The propagation of the GPS signal in the neutral atmosphere is a function of the refractive index, which depends on the temperature, pressure, and water vapor content of the atmosphere. Water vapor creates a delay due to the asymmetric distribution of charge in the water vapor dipole. The total neutral atmospheric delay is divided into two parts: the **wet delay** which is caused by the water

molecule dipole effect as described above, and the **hydrostatic delay** which is caused by nondipole components of the refractivity of water vapor. These delays are at a minimum along the zenith direction, and increase inversely with the sine of the elevation angle.

The Zenith Hydrostatic Delay (known as ZHD) is found using a surface pressure measurement along with a mapping function and is given by (Bevis et al., 1992):

$$ZHD = (2.2779 + /- 0.0024) * P / f(\lambda, H) \quad (3.12)$$

where P is the surface pressure in millibars, and $f(\lambda, H)$ is the variation in the gravitational acceleration with latitude λ and height H and is given by (Bevis et al., 1992):

$$f(\lambda, H) = (1 - 0.00266 * \cos 2\lambda - 0.00028 * H) \quad (3.13)$$

The height and latitude dependence in Equations 3.12 and 3.13 comes from the height and latitude dependence of the acceleration of gravity. Particles that are either near the equator or high in the atmosphere experience less downward acceleration and thus remain in the atmosphere longer. This creates a greater effect on the GPS signal delay.

Once the ZHD has been calculated, the Zenith Wet Delay (ZWD) can be extracted by subtracting the ZHD from the Zenith Tropospheric delay (ZTD). The ZTD is calculated by constraining the positions of a network of GPS receivers and then measuring the position error. System-related errors are systematically removed, and the remaining error is assumed to come from the neutral atmosphere delay. The ZWD is approximately proportional to the integrated water vapor in the

atmospheric column directly above the GPS site. The integrated water vapor is given by:

$$IWV = \Pi * ZWD \qquad (3.14)$$

$$\text{where } \Pi = 10^6 \Big/ \left(\rho * R_v * \left[\left(k_3/T_m\right) + k_2'\right]\right) \qquad (3.15)$$

$$\text{and } k_2' = k_2 - m * k_1 \qquad (3.16)$$

$$\text{and } T_m = 0.72 * T_s + 70.2 \qquad (3.17)$$

where ρ is the density of liquid water, R_v is the gas constant for water vapor, T_m is the weight mean temperature of the atmosphere, m is the ratio of the molar mass of water vapor to the molar mass of dry air, T_s is the surface temperature, and the physical constants k_1, k_2, and k_3 are derived from the expression for atmospheric refractivity:

$$N = k_1\left(P_d/T\right) + k_2\left(P_v/T\right) + k_3\left(P_v/T^2\right) \qquad (3.18)$$

P_d and P_v are the partial pressures of dry air and water vapor and T is absolute temperature (Bevis et al., 1993). The constants (ρ, R_v, and m) are all assumed to be well known to a high degree of accuracy, and thus have a limited impact on the uncertainties of Π. The uncertainties are derived from T_m, k_1, k_2, and k_3. The coefficients k_n are considered to be measured with a high amount of certainty, therefore narrowing down the error to the T_m term.

The TPW is easily calculated from the IWV through the following relation (Bevis et al., 1992; Bevis et al., 1993):

$$IWV = \rho * TPW \qquad (3.19)$$

Anywhere from four to ten satellites may be used to measure TPW from a ground-based GPS receiver, which results in highly accurate measurements. The delay of each satellite signal is calculated and then mapped onto the zenith. The TPW for each signal is then calculated, after which all of the TPW measurements are averaged in order to get the final TPW product. The GPS-TPW measurement is a volume average which is taken over a cone shape with its apex pointed downward, with a height of 5.0 km, a base of 21 km, and a total volume of nearly 580 km^3 (see Figure 3.7).

Although the GPS measurement of TPW is highly accurate, various sources of error do exist. The largest source of error comes from the calculation of the surface pressure. Pressure sensors at the ground-based receiver sites typically have an accuracy of about 0.1 hPa. This measurement is also converted into sea-level pressure from the GPS antenna height. After this conversion has been performed, the total pressure error is typically less than 0.3 hPa. This leads to a TPW error of about 1 mm.

Other error sources are present in the TPW calculation, such as in the calculation of T_m, however these sources do not contribute significantly to the overall error or 1 mm (Bevis et al, 1993).

Of the thousands of ground based GPS sites across the world, over 300 are currently located over the United States. These ground stations are predominately run by four agencies: the National Oceanic and Atmospheric Administration (NOAA), Suominet, the United States Coast Guard, and the United States

Department of Transportation. Figure 3.8 shows the distribution of GPS sites across the United States (NOAA FSL GPS-Met Observing Systems Branch, 2005).

AMSU-B main beam efficiencies			
Channel	Freq (GHz)	Pixel	Efficiency
16	89.0	45	94.4
17	150.0	45	95.1
18	183.3	45	95.1
19	183.3	45	96.9
20	183.3	45	96.9
AMSU-B widebeam efficiencies			
Channel	Freq (GHz)	Pixel	Efficiency
16	89.0	45	98.36
17	150.0	45	99.45
18	183.3	45	99.45
19	183.3	45	99.64
20	183.3	45	99.64

Figure 3.1: Measured NOAA-15 AMSU-B mainbeam and widebeam antenna efficiencies along with their corresponding frequency.

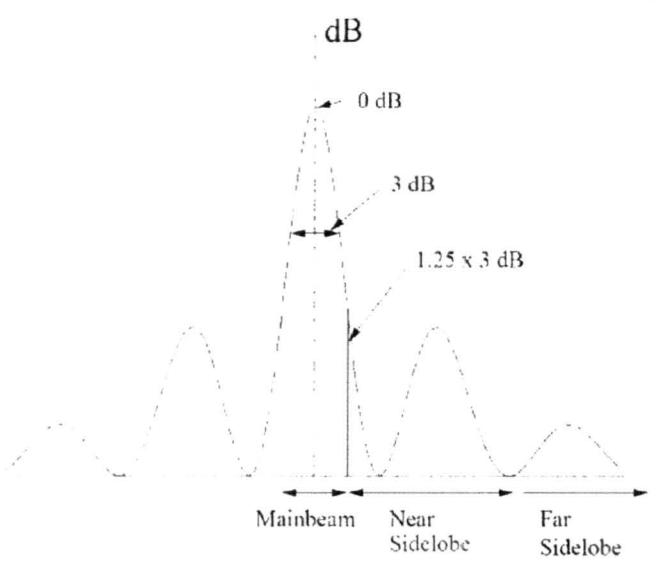

Figure 3.2: A schematic of a typical antenna gain pattern. The mainbeam is defined as 1.25 times the 3 db width. The near and far sidelobes are jointly referred to as the sidelobe.

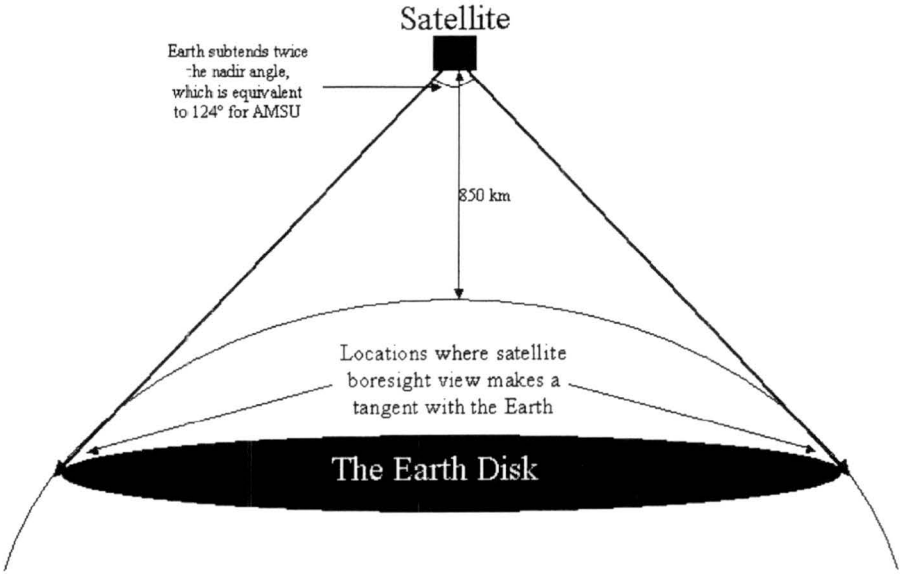

Figure 3.3: A physical representation of the "Earth Disk" that the satellite sees.

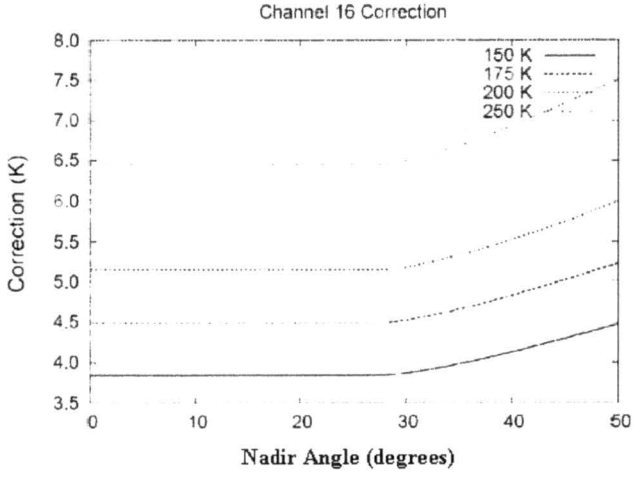

Figure 3.4: The antenna pattern corrections for AMSU-B channel 16. Corrections are constant for view angles less than 28. Above this, the earth begins to become subtended by the satellite platform.

Retrieved Variable	Mean Difference* (variable units)	Mean Difference* (%)
Surface temperature	0.52 K	0.1
23 GHz emissivity	-0.007	-1.4
31 GHZ emissivity	-0.007	-1.3
50-60 GHz emissivity	-0.007	-1.3
89 GHz emissivity	-0.007	-1.1
183 GHz emissivity	-0.007	-0.9
300 hPa mixing ratio	0.002 g/kg	10.6
500 hPa mixing ratio	0.013 g/kg	14.8
700 hPa mixing ratio	0.061 g/kg	9.3
850 hPa mixing ratio	0.43 g/kg	6.9
1000 hPa mixing ratio	0.79 g/kg	5.7
300 hPa temperature	0.35 K	0.2
500 hPa temperature	0.37 K	0.1
700 hPa temperature	0.41 K	0.1
850 hPa temperature	0.34 K	0.1
1000 hPa temperature	0.32 K	0.1

* with AMSU-B APC minus without AMSU-B APC.

Figure 3.5: Effect of the AMSU-B APC on surface emissivity, temperature, and mixing ratio retrievals.

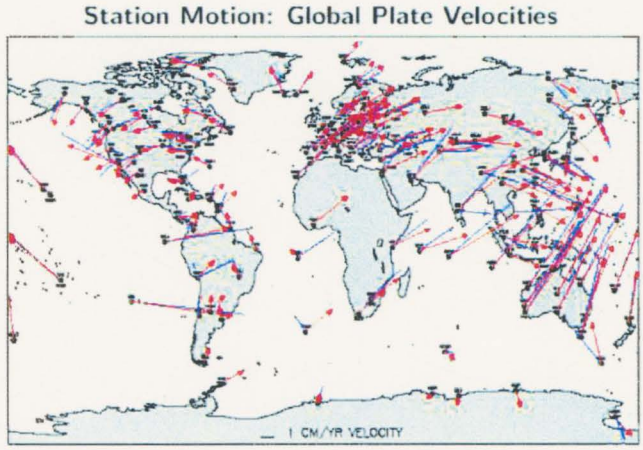

GPS velocities (red) are in good agreement with long-term geophysical velocities (blue) derived from paleomagnetic data and hot spots.

Figure 3.6: A global map of plate velocities. Most velocities are less than about 2 cm/yr (Rothacher, 2005).

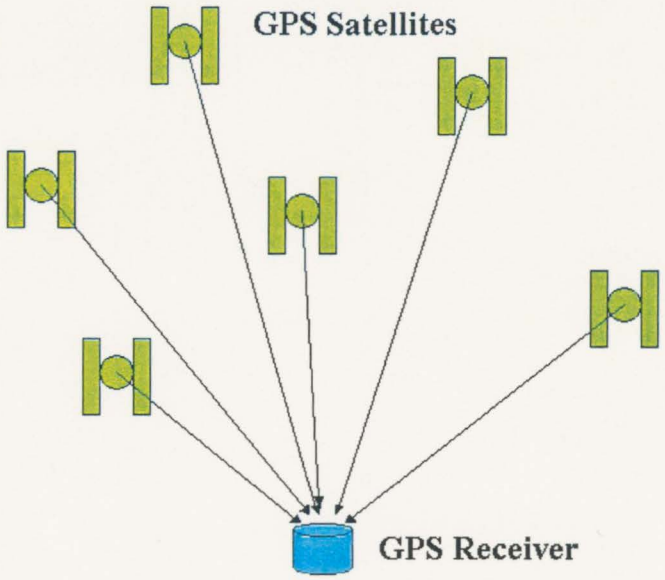

Figure 3.7: Scalar precipitable water is obtained by averaging vector zenith-mapped slant delays.

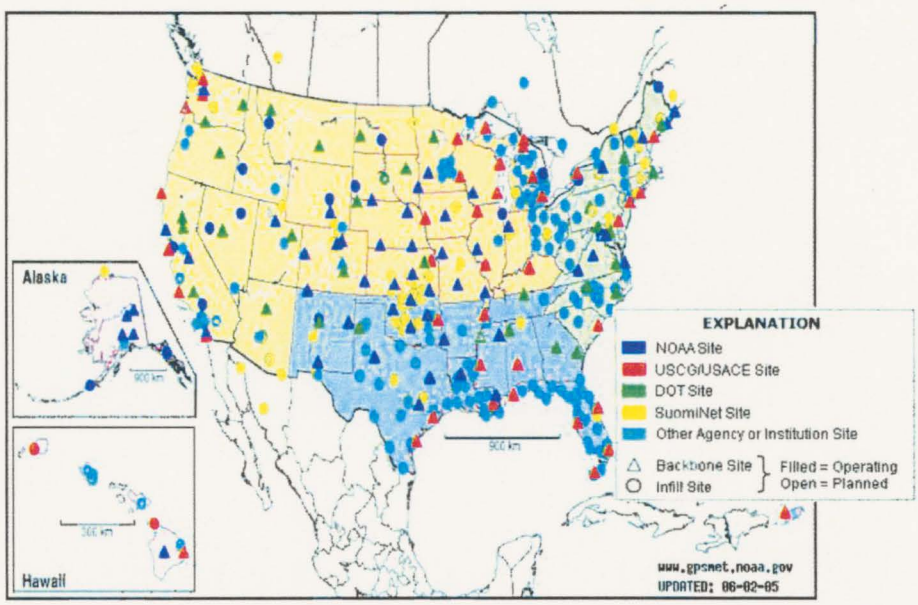

Figure 3.8: A map of the GPS stations over CONUS.

CHAPTER 4: WATER VAPOR RETRIEVAL

4.1 An Introduction to Inverse Problems

Due to the expensive and difficult nature of directly sensing the atmosphere globally, remote sensing methods have been developed. Remote sounding of the atmosphere has been carried out by a wide variety of instruments, using many different principles of measurement. Almost all techniques involve the measurement of electromagnetic radiation, although sound propagation has also been used. Electromagnetic measurements involve the refraction, transmittance, scattering, and thermal emission of radiation at all wavelengths from radio to the ultraviolet.

These remote measurements, however, often lead to interpretation problems that are known as Inverse Problems. The nature of inverse problems can be better understood through the use of a "footprint" analogy. For example, it is very easy to determine what kind of a footprint an animal would leave if the type of animal were known. For inverse problems, however, the type of animal must be determined solely by its footprint. There are many things that can be inferred about the animal based on the depth and size of the print, but it is impossible to pull out some types of information, such as fur color for example. This is the ill-posed nature of the inverse problem. In order to add information, constraints are put on the system in order to narrow down the number of solutions to only those that are probable and

physical. For example, we could add a constraint that states that the fur color cannot be orange, purple, or pink.

The general inverse problem in remote sensing involves setting up and solving a set of simultaneous linear or non-linear equations. Complications arise due to the presence of experimental error in some of the parameters, and also due to the presence of approximations in the formulation of the equations.

The retrieved parameters are represented by a state vector, x, with n elements, $x_1, x_2, \ldots, x_n$. The state vector represents the profile of an unknown quantity to be retrieved at a set number of levels such that the profile can represent the vertical atmospheric variations. The state vector used in this research contains 20 elements, which will be described in Chapter 5.

The parameters that are directly measured in order to retrieve x are represented by the measurement vector y, with m elements, $y_1, y_2, \ldots, y_m$. This vector contains all of the quantities measured that are functions of the state vector. Typically a quantity that appears in the measurement vector will only appear in the state vector if a direct measurement is taken of that quantity. Due to the fact that measurements can only be made to a finite accuracy, error and noise are present in the measurement vector.

For each state vector there exists a corresponding ideal measurement vector, y_I, determined by the physics of the measurement (Rodgers, 2000). The physics is described by the forward function $f(x)$:

$$y_I = f(x) \qquad (4.1)$$

Along with the experimental error comes error due to the approximations made in the physics of the forward model. We can express the relationship between the measurement vector and the state vector more accurately by introducing a term (ε) to describe these errors (Rodgers, 2000):

$$y_I = f(x) + \varepsilon \qquad (4.2)$$

There are two main ingredients needed in order to build a forward model: knowledge of the instrument and how it works, and a firm understanding of how the measured quantity relates to the desired quantity. The latter of the two involves the forward model *f(x)* and understanding where the model is making assumptions, as well as being able to decipher the physics itself.

Another issue that arises when dealing with inverse problems is that the parameters to be retrieved are expressed by continuous functions, whereas measurements are only taken over discrete space. This results in most inverse problems being ill posed or under-constrained. To deal with this problem, the true continuous state function with its infinite number of variables is represented as a finite number of discrete points. This can be done in any number of ways, and is dependent on the resolution and degree of accuracy desired for the particular scientific application. After the problem has been discretized, the problem may or may not be under-constrained, depending on the grid spacing required and the information content of the measurement (Rodgers, 2000).

4.2 The Forward Radiative Transfer Model

The radiative transfer model that was employed for this retrieval is based on the work of Deeter and Evans (1998) and describes a scattering layer in a plane-parallel thermally emitting atmosphere. The model is designed specifically for radiance computing in iterative remote sensing schemes. This model is a combination of a single-scatter method along with Eddington's second approximation technique.

Due to the vast amount of data that must be processed during a retrieval, computational efficiency becomes highly important. When approximate solutions are used in place of the "exact" solutions, the computation time is greatly reduced. For example, not allowing scattering in the field of view of the instrument does not greatly affect the overall accuracy of the measurement (scattering in the microwave spectrum is several orders of magnitude less likely than absorption and emission). By removing scattering from the radiative transfer equations, the computation time becomes reduced. This allows for faster data flow between the satellite data processing centers and the data assimilation centers and forecast modelers. There is a tradeoff between processing time and accuracy, however the delta-Eddington second approximation increases accuracy without greatly effecting the computation time.

The radiative transfer equation is given by:

$$\mu \frac{dI}{d\tau} = I(\tau,\mu) - J(\tau,\mu) = I(\tau,\mu) - \left[\frac{\omega}{2} \int_{-1}^{1} I(\tau,\mu') P(\mu,\mu') d\mu' + B(\tau)(1-\omega) \right]$$

(4.3)

where $I(\tau,\mu)$ is the radiance, τ is the optical depth, μ is the cosine of the radiance's zenith angle, $J(\tau,\mu)$ is the source function, ω is the single-scattering albedo, $P(\mu,\mu')$ is the scattering phase function, and $B(\tau)$ is the Planck function (Deeter and Evans, 1998). This radiative transfer equation assumes azimuthal symmetry. The Eddington solution to the radiative transfer equation is computationally inexpensive due to the fact that the μ-dependence of the radiance field and scattering phase function is approximated with first-order polynomials. These approximations take on the forms:

$$I_E(\tau,\pm\mu) \approx \frac{1}{2}\left[(2 \pm 3\mu)F^+(\tau) + (2 \mp 3\mu)F^-(\tau)\right] \quad (4.4)$$

and

$$P_E(\mu,\mu') \approx 1 + 3g\mu\mu' \quad (4.5)$$

where $F^+(\tau)$ and $F^-(\tau)$ are the upwelling and downwelling fluxes, and g is the asymmetry parameter associated with the phase function (Deeter and Evans, 1998).

4.3 Optimal Estimation

The relationship between the measured radiances and the state vector is given by:

$$y = f(x,b) + \varepsilon_y \quad (4.6)$$

where b is a vector containing model parameters that act as a constraint on the solution, x is the state vector, y are the measured radiances, and ε_y is the

measurement error. Linearizing Equation 4.6 about the real state vector profiles and the real model parameters gives :

$$y(\hat{x},\hat{b}) = F(x,b) + \frac{\partial F}{\partial x}(\hat{x} - x) + \frac{\partial F}{\partial b}(\hat{b} - b) + \varepsilon_y \qquad (4.7)$$

where $\hat{x}$ contains the estimated water vapor and temperature profiles, along with emissivity at five frequencies, and $\hat{b}$ is the estimated model parameter vector (Engelen and Stephens, 1999). The terms containing the derivative of the forward model ($\frac{\partial F}{\partial b}$ and $\frac{\partial F}{\partial x}$) are the sensitivities of the radiances to deviations in the model parameters and the water vapor profile, respectively. Sensitivities will be further discussed in Chapter 5.

In order to obtain the retrieved water vapor profile from the measurements, the inverse model, *I*, is used. The linearized equation for the inverse model is given by:

$$\hat{x} = I(y,b) + \frac{\partial I}{\partial y}(\hat{y} - y) + \frac{\partial I}{\partial b}(\hat{b} - b) \qquad (4.8)$$

The sensitivity of the retrieved water vapor profile to the measurement errors described by $\frac{\partial I}{\partial y}$ is referred to as the contribution function and is denoted by D_y (Engelen and Stephens, 1999).

Due to the fact that the inversion of the forward model is extremely sensitive to noise, a constraint is needed in order to arrive at the optimal solution. Optimal estimation uses a priori profiles as virtual measurements in order to provide these constraints. The optimal solution is obtained by minimizing a cost function given by:

$$\Phi = (x - x_a)^T S_a^{-1}(x - x_a) + (y - F(\hat{x}))^T S_y^{-1}(y - F(\hat{x})) \qquad (4.9)$$

where x_a is the a priori profile and S_a and S_y are the error covariance matrices of the a priori data and the forward model which contain elements of b (Engelen and Stephens, 1999). The source for these came from the NOAA-88 sounding dataset, and an example of the correlations can be found in Figure 4.2. Minimizing the solution and solving for the estimated water vapor profile yields:

$$\hat{x} = x_a + S_a K^T S_y^{-1}(y - F(\hat{x})) \qquad (4.10)$$

where K is the Kernel matrix (also known as the Jacobian) and defines the sensitivity of the forward model to perturbations in the parameter being retrieved (see Chapter 5).

4.4 C1DOE Retrieval

This retrieval method is referred to as C1DOE and is currently under development at the Cooperative Institute for Research in the Atmosphere (CIRA), and was applied to AMSU-A and B data to produce temperature, emissivity, and water vapor fields. The information that is passed in to the retrieval from AMSU consists of scan time, brightness temperatures for all 20 channels, surface type, zenith angle, scan position, and emissivities at 23, 31, 89, and 150 GHz.

First guess data for each of the retrieved fields comes from a variety of sources. The Agricultural Meteorology modeling system developed by the United States Air Force (AGRMET) provided a three-hour, global a priori dataset for surface temperature as well as providing a few currently unused fields, such as soil

moisture, surface topography, vegetation coverage, snow depth, soil type, and a three hour average of surface temperature. The Microwave Emissivity Model (see Chapter 2) provided first guess information for emissivity at five channels (23, 31, 50, 89, 150 GHz). The water vapor profile first guess came from a global radiosonde match-up dataset that included a set of vital statistics and configuration information, and a second set of meteorological data. All of the first guess information was used to construct the a priori database as well.

The C1DOE retrieval outputs a mixing ratio and temperature profile for 7 pressure levels (1000, 850, 700, 500, 300, 200, and 100mb) as well as providing a total column water vapor measurement (TPW). Emissivities are calculated at 5 frequency bands (23, 31, 50, 89, 150 GHz). The retrieval will soon have the capability to output cloud liquid water. Figure 4.1 shows the data flow through the C1DOE routine.

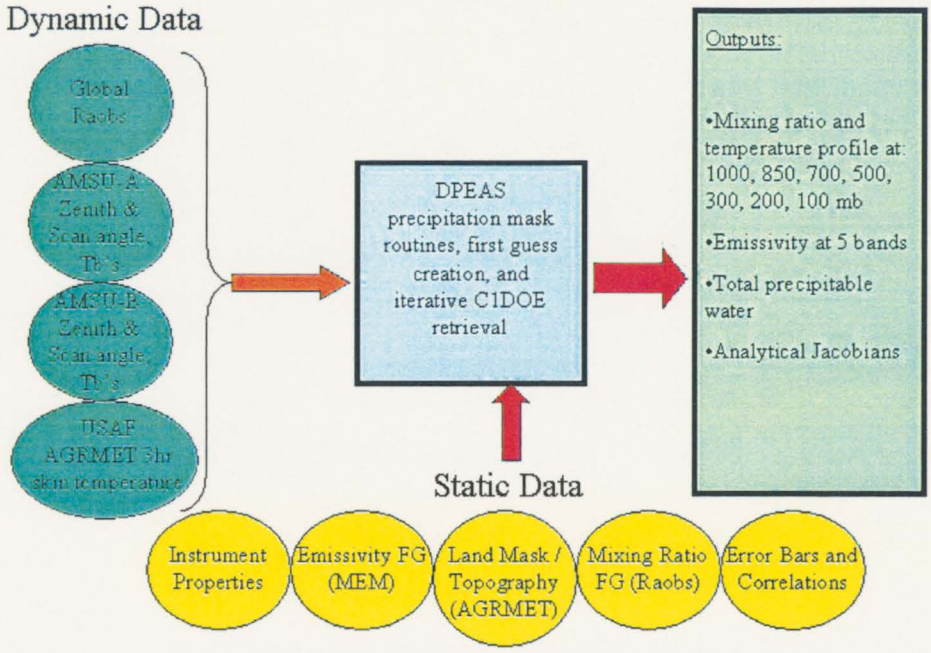

Figure 4.1: The current data flow through the C1DOE algorithm.

Clear Correlation Matrix (McKague's)

	E23	E31	E50	E89	E150	E183	q100	q200	q300	q500	q700	q850	q1000	T100	T200	T300	T500	T700	T850	T1000
E 23	1.00	0.99	0.99	0.96	0.92	0.89	-0.32	-0.36	-0.37	-0.50	-0.64	-0.80	-0.84	0.19	-0.28	-0.66	-0.74	-0.76	-0.90	-0.86
E 31	0.99	1.00	0.99	0.97	0.93	0.90	-0.34	-0.39	-0.39	-0.53	-0.67	-0.83	-0.87	0.20	-0.29	-0.68	-0.77	-0.79	-0.92	-0.89
E 50	0.98	0.99	1.00	0.99	0.95	0.92	-0.37	-0.41	-0.42	-0.56	-0.69	-0.87	-0.91	0.23	-0.29	-0.71	-0.79	-0.82	-0.94	-0.89
E 89	0.96	0.97	0.99	1.00	0.98	0.96	-0.40	-0.43	-0.44	-0.59	-0.82	-0.89	-0.74	0.27	-0.28	-0.72	-0.79	-0.81	-0.93	-0.87
E 150	0.92	0.93	0.95	0.98	1.00	0.99	-0.39	-0.42	-0.42	-0.55	-0.80	-0.66	0.70	0.29	-0.25	-0.67	-0.73	-0.75	-0.76	-0.79
E 183	0.89	0.90	0.92	0.96	0.99	1.00	-0.37	-0.40	-0.40	-0.52	-0.67	-0.62	-0.66	0.29	-0.22	-0.62	-0.68	-0.69	-0.71	-0.73
q 100	-0.32	-0.34	-0.37	-0.40	-0.39	-0.37	1.00	0.98	0.98	0.69	0.57	0.58	0.60	-0.32	0.24	0.61	0.55	0.50	0.48	0.46
q 200	-0.36	-0.39	-0.41	-0.43	-0.42	-0.40	0.98	1.00	1.00	0.69	0.58	0.59	0.60	-0.31	0.29	0.66	0.58	0.54	0.51	0.50
Q 300	-0.37	-0.39	-0.42	-0.44	-0.42	-0.40	0.98	1.00	1.00	0.69	0.58	0.59	0.60	-0.32	0.27	0.66	0.59	0.55	0.52	0.50
Q 500	-0.50	-0.53	-0.56	-0.58	-0.55	-0.52	0.69	0.69	0.69	1.00	0.81	0.78	0.76	-0.40	0.19	0.70	0.74	0.72	0.70	0.67
Q 700	-0.64	-0.67	-0.69	-0.82	-0.80	-0.67	0.57	0.58	0.58	0.81	1.00	0.86	0.84	-0.40	0.21	0.70	0.75	0.75	0.75	0.72
Q 850	-0.80	-0.83	-0.87	-0.89	-0.86	-0.82	0.58	0.58	0.59	0.78	0.86	1.00	0.94	-0.45	0.24	0.77	0.81	0.81	0.80	0.80
Q 1000	-0.84	-0.87	-0.71	-0.74	-0.70	-0.66	0.60	0.60	0.60	0.78	0.84	0.94	1.00	-0.47	0.25	0.81	0.86	0.86	0.85	0.86
T 100	0.19	0.20	0.23	0.27	0.29	0.29	-0.32	-0.31	-0.32	-0.40	-0.40	-0.45	-0.47	1.00	0.47	-0.29	-0.39	-0.39	-0.34	-0.30
T 200	-0.28	-0.29	-0.29	-0.28	-0.25	-0.22	0.24	0.29	0.27	0.19	0.21	0.24	0.25	0.47	1.00	0.52	0.28	0.26	0.28	0.32
T 300	-0.66	-0.68	-0.71	-0.72	-0.67	-0.62	0.61	0.66	0.66	0.70	0.70	0.77	0.81	-0.29	0.52	1.00	0.89	0.85	0.83	0.82
T 500	-0.74	-0.77	-0.79	-0.79	-0.73	-0.68	0.55	0.58	0.59	0.74	0.75	0.81	0.86	-0.39	0.28	0.89	1.00	0.98	0.94	0.91
T 700	-0.76	-0.79	-0.32	-0.81	-0.75	-0.69	0.50	0.54	0.55	0.72	0.75	0.81	0.86	-0.38	0.26	0.85	0.98	1.00	0.98	0.94
T 850	-0.90	-0.92	-0.94	-0.93	-0.76	-0.71	0.48	0.51	0.52	0.70	0.75	0.80	0.85	-0.34	0.28	0.83	0.94	0.98	1.00	0.96
T 1000	-0.86	-0.88	-0.89	-0.87	-0.79	-0.73	0.46	0.50	0.50	0.67	0.72	0.80	0.86	-0.30	0.32	0.82	0.91	0.94	0.96	1.00

Figure 4.2: The correlation matrix used in the C1DOE retrieval (McKague et al., 2001; McKague et al., 2003).

CHAPTER 5: SENSITIVITES

5.1 The Analytical Jacobian

Much can be learned about the performance of the retrieval by making use of derivatives of the forward model. For a large and complicated model, such as the C1DOE, an easy and effective way to evaluate the forward model is to re-evaluate the derivatives, also known as Jacobians, obtained by perturbing the state vectors by small amounts. Given a set $y = f(x)$ of n equations of n variables $x_1,\ldots, x_n$, the Jacobian matrix can be mathematically described by Equation 5.1:

$$J(x_1,\ldots,x_n) = \begin{bmatrix} \frac{dy_1}{dx_1} & \cdots & \frac{dy_1}{dx_n} \\ \vdots & \ddots & \vdots \\ \frac{dy_n}{dx_1} & \cdots & \frac{dy_n}{dx_n} \end{bmatrix} \quad (5.1)$$

In order to improve the speed of the retrieval, the Jacobian is approximated and thus is referred to as an analytical Jacobian. While the analytical fit introduces small errors, these are essentially negligible (less than 10%).

The analytical Jacobian gives information on the sensitivity of the forward model to changes in the state vector. This information gives the user a sense of how well both the retrieval and the instrument can ultimately perform by showing which variables have a meaningful signal and which ones do not. It also provides insight as to which channels would be best suited to retrieve certain parameters. This

serves as a very helpful and skillful way to approach sensor design and channelization setup. Analytical Jacobians are also used for evaluating the physics of the forward model by analyzing how state vector parameters change under varying circumstances. The state vector in this work consists of 20 elements that can be retrieved, and includes a skin temperature, mixing ratio and temperature at 7 levels (100, 200, 300, 500, 700, 850, and 1000 mb), and five emissivities (23, 31, 50, 89, and 150 GHz). The Jacobian examines the sensitivities to these 20 elements at 13 frequencies (see Figure 5.1). Seven of the channels around the 60 GHz oxygen absorption band have been removed as they exhibit no sensitivity to water vapor, which is the focus of this study. Only one channel in this portion of the spectrum has been retained (55.5 GHz) in order to illustrate this effect. It should be noted that these channels do become very important for temperature profiling.

Figure 5.1 is an example of the Jacobian matrix for a mid-latitude atmosphere with marginal values of water vapor. This matrix shows which channels have the best sensitivities to given parameters. For skin temperature, six of the thirteen frequencies have no sensitivity whatsoever (channels near the 60 GHz oxygen absorption band, and the water vapor profiler channels). The 31.4 GHz channel has the highest sensitivity due to the fact that it is a window channel. The emissivities are frequency dependent, so they are sensitive accordingly (e.g. the emissivity at 50 GHz, is sensitive only to frequencies at or very near 50 GHz, and has zero sensitivity elsewhere). For water vapor, the highest sensitivities are at the 183 GHz channels, however signal exists for all other channels besides the 50-60 GHz channels. For example, the 150 GHz channel has a Jacobian value of 4.96 with

respect to the 850 mb mixing ratio. This means that if 1 g/kg of water vapor were added at 850 mb, the brightness temperature would go up by 4.96 K, which is significantly above the NEΔT of 0.84 K for AMSU. The water vapor signals are also far stronger than the temperature sensitivities, which are generally near or lower than the instrument noise level at these frequencies.

Two atmospheric states were chosen as the focus of this sensitivity study. A dry and moist atmospheric water vapor profile were picked and run through the retrieval at varying emissivities. These profiles came from a radiosonde match-up dataset that consisted of 277 data points. These two profiles represent the driest and the wettest of all 277 cases. Figures 5.2-5.5 show the temperature and moisture profiles for both cases. These profiles came from the radiosonde match-up data set, and have 26 temperature levels and 7 mixing ratio levels. The two profiles have similar temperature structure below the stratopause, however the dry case has a lower magnitude than the wet profile. The tropopause height is also much lower for the dry case, most likely due to the colder tropospheric air mass. The moisture profiles have slightly different forms, however the wet case has mixing ratios on the order of five times larger than the dry case.

Figures 5.6 - 5.13 show vertical profiles of sensitivity at four different values of emissivity for dry and wet atmospheric conditions. The emissivity values range from a typical ocean background (e=0.5), to a possible ocean land mix (e=0.7), to a typical land emissivity signature (e=0.9), and finally to a highly emitting land background (e=0.99). Six channels were used in this emissivity study, spanning the microwave spectrum: 23.8 GHz, 55.5 GHz, 89.0 GHz, 150 GHz, and two

broadband water vapor profiling channels with a central frequency of 183 GHz. The profiles are composed of analytical Jacobian calculations made at seven pressure levels: 1000, 850, 700, 500, 300, 200, and 100 mb. The 55.5 GHz channel exhibited no sensitivity to water vapor due to its proximity to the oxygen absorption line, and thus is plotted only once, and will not be mentioned hereafter.

Figure 5.6 shows high values of sensitivity to the surface conditions at all channels when the emissivity is set to 0.5 for the dry atmospheric case. The 150 GHz channel has the highest sensitivity because its weighting function is near its peak at the surface. The 183 GHz channels have peaks that are higher in the atmosphere and, thus, resemble true sounding channels. Another reason that the Jacobian is more sensitive to upper tropospheric water vapor is because 1 g/kg is a much larger change at 300 mb than it is at 850 mb for example.

Figure 5.7 shows the wet case for the 0.5 emissivity case. All of the frequencies with the exception of the 23 GHz channel show less sensitivity, and the 150 GHz channel starts resembling a sounding channel. One explanation for this is due to the fact that 1 g/kg of water vapor is a smaller percentage of change for the wet case than for the dry. The 89 GHz also begins to show more atmospheric attenuation effects, giving it lower signal in the higher atmosphere.

Next, the emissivity was increased to 0.7. This resulted in a similar structure to the previous case, however the magnitudes are slightly lower throughout the whole depth of the atmosphere (see Figure 5.8). The signal in the lower troposphere, however, is still strong. The 183 GHz channels actually gained some signal in the higher atmospheric regions.

For the wet case, the magnitudes are similarly decreased from the 0.5 emissivity case as seen in Figure 5.9. The 150 GHz channel exhibits even more sounding characteristics, as its sensitivity in the upper troposphere tends to be negative and begins to increase in magnitude.

Once the emissivity reaches 0.9 (more typical of land scenes), all channels except for the 183 GHz lose signal above 700 mb in the dry case (see Figure 5.10). The wet case shows significantly reduced emissivity values. However, the signal is still larger than the instrument noise (see Figure 5.11). All of the channels tend to have negative sensitivities in the upper troposphere.

Finally, an emissivity of near 1 (e=0.99) still shows sensitivities of between 2 and 9 K/(g/kg) for three channels (23, 89, 150, and 183 GHz) for the dry case (see Figure 5.12). The 183 GHz channels continue to show a slight increase in sensitivity. The wet case shows a significant decrease in sensitivities yet still retains a decent signal (see Figure 5.13). The 183 GHz channels continue to gain signal in the upper troposphere.

Figures 5.14-5.19 show how the sensitivities at chosen frequencies change as the emissivity goes from 0.5 to 1.0. Three atmospheric pressure levels were chosen for this study: 100, 500, and 1000 mb. Only one of the 183 GHz channels is shown for most of these plots, due to the fact that these channels have very high values, and make the imaging channels difficult to interpret. Sensitivities with a flat slope (slope is near or at zero) when plotted against emissivity are preferred, because this means that the retrieval is less dependent on the accuracy of the surface emissivity measurement.

For the dry case at 100 mb, all sensitivities have negative slopes, and all but the 183 GHz channel goes from a positive to a negative value (see Figure 5.14). Consequently, the 183 GHz channels are the only frequencies to retain signal that is above the noise level (see Figure 5.20 for NEΔT values for all channels). The wet case is very similar, however the lower frequency channels have even less signal (see Figure 5.15). The 150 GHz channel begins to pick up more signal. However, it is still slightly below the instrument noise level and, thus, does not contribute to the information content of the retrieval either.

At 500 mb, for the dry case, there are much higher sensitivities, however most of the lines go below the 0.5 K threshold (the lowest of the NEΔT values) at around e=0.83 and lose signal (see Figure 5.16). The curves are much steeper in this case, which denotes that the Jacobian is more sensitive to emissivity at this level. The 183 GHz channel seems to improve as it approaches the higher emissivities, which is helpful as all other channels lose signal at high emissivities. The wet case showed reduced sensitivities. However, the curves are much shallower (see Figure 5.17). The 150 GHz channel begins to pick up a stronger negative signal as emissivity approaches 1. The 183 GHz channel seems to have no sensitivity to the emissivity changes, and retains a decent signal throughout the emissivity range. The 89 GHz channel loses signal above e=0.66, and the 23 GHz channel loses signal above e=0.76.

Near surface pressure for the dry case, all channels shown have shallow lines and good signal (see Figure 5.18). The loss of signal between e=0.5 and e=1 is about 40%, but the sensitivity in all channels still remains high enough to overcome

instrument noise. The wet case shows dramatically reduced magnitudes (see Figure 5.19). The slopes are again shallow, and three of the channels remain above the noise level (23, 89, and 150 GHz).

Sensitivity is lost as the emissivity approaches unity, particularly during wetter conditions (sensitivity was considered null when the Jacobian values were less than the corresponding NEDT values for the particular channel). However, there existed no area where all of the channels had sensitivities that were identically zero. In the upper atmosphere, when the imaging channels lose all signal, the sounding channels retain good strength. Conversely, at the surface, when the profiling channels lose signal, the imaging channels retain abundant sensitivity. In the middle and lower atmosphere, all channels (except the profilers) had a strong sensitivity to emissivity, which calls for a need to have more accurate emissivity measurements. Sensitivities of the Jacobian to emissivity ranged from 0.33 K to 1.0 K per tenth of a unit of emissivity. With the existence of the profiling channels, however, little to no knowledge of the surface emissivity can still lead to a meaningful mid to upper tropospheric retrieval as shown.

Jacobian

	Tskin	e23	e31	e50	e89	e150	q100	q200	q300	q500	q700	q850	q1000	T1	T2	T3	T4	T5	T6	T7
23.8 GHz	0.42	207.02	0.00	0.00	0.00	0.00	0.15	0.42	1.17	1.98	1.94	2.24	2.50	0.00	0.00	0.00	0.01	0.02	0.01	0.01
31.4 GHz	0.46	0.00	253.75	0.00	0.00	0.00	0.03	0.08	0.24	0.53	0.71	1.11	1.45	0.00	0.00	0.00	-0.01	-0.02	-0.06	-0.10
50.3 GHz	0.34	0.00	0.00	139.53	0.00	0.00	0.01	0.05	0.17	0.43	0.62	1.20	1.70	0.01	0.01	0.01	0.00	-0.02	-0.10	-0.17
52.8 GHz	0.16	0.00	0.00	33.61	0.00	0.00	-0.02	-0.03	-0.01	0.06	0.13	0.48	0.77	0.03	0.06	0.11	0.17	0.15	0.19	0.22
53.48-53.71 GHz	0.06	0.00	0.00	6.46	0.00	0.00	-0.03	-0.05	-0.04	-0.02	0.01	0.16	0.29	0.04	0.10	0.18	0.23	0.17	0.34	0.48
54.4 GHz	0.01	0.00	0.00	0.33	0.00	0.00	-0.03	-0.04	-0.03	-0.02	0.00	0.02	0.04	0.09	0.18	0.26	0.23	0.11	0.43	0.71
54.94 GHz	0.00	0.00	0.00	0.02	0.00	0.00	-0.02	-0.03	-0.01	-0.01	0.00	0.00	0.01	0.16	0.26	0.25	0.17	0.05	0.46	0.82
55.5 GHz	0.00	0.00	0.00	0.00	0.00	0.00	-0.01	-0.01	0.00	0.00	0.00	0.00	0.00	0.24	0.32	0.18	0.07	0.01	0.48	0.89
89.0 GHz	0.38	0.00	0.00	0.00	171.96	0.00	0.07	0.20	0.65	1.55	2.23	3.92	5.38	0.00	0.00	0.00	-0.02	-0.07	-0.28	-0.46
150 GHz	0.22	0.00	0.00	0.00	0.00	59.79	-0.18	-0.21	0.20	1.18	2.14	4.96	7.39	0.00	0.00	0.01	0.03	0.04	-0.15	-0.31
182.31-184.31 GHz	0.00	0.00	0.00	0.00	0.00	0.00	-61.85	-80.54	-35.58	-8.26	0.00	0.00	0.00	0.01	0.06	0.42	0.49	0.12	0.50	0.83
180.31-186.31 GHz	0.00	0.00	0.00	0.00	0.00	0.00	-10.47	-16.19	-13.29	-6.51	-0.24	0.00	0.00	0.00	0.01	0.18	0.51	0.36	0.52	0.66
176.31-190.31 GHz	0.01	0.00	0.00	0.00	0.00	0.12	-2.60	-4.26	-4.43	-3.19	-0.82	-0.06	0.00	0.00	0.00	0.06	0.32	0.44	0.66	0.85

Figure 5.1: An example case of the Jacobian matrix. Null values are denoted in pink. Units of the Jacobian are in (K/K) for all temperatures, (K/(g/kg)) for mixing ratio, and (K) for emissivity.

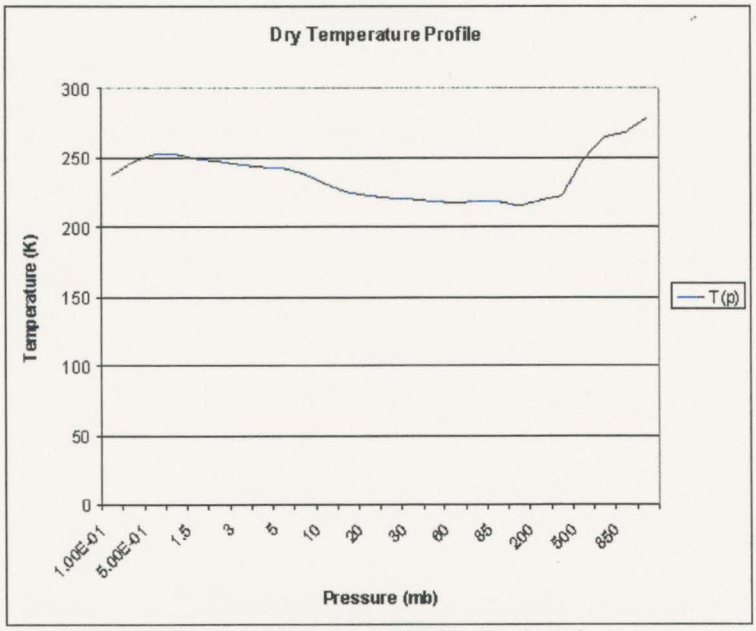

Figure 5.2: The temperature profile for the "dry" case.

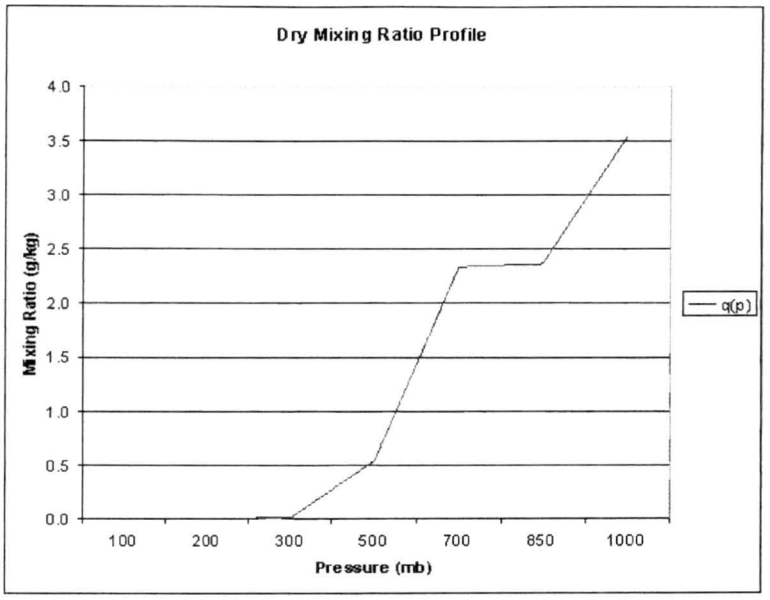

Figure 5.3: The mixing ratio profile for the "dry" case.

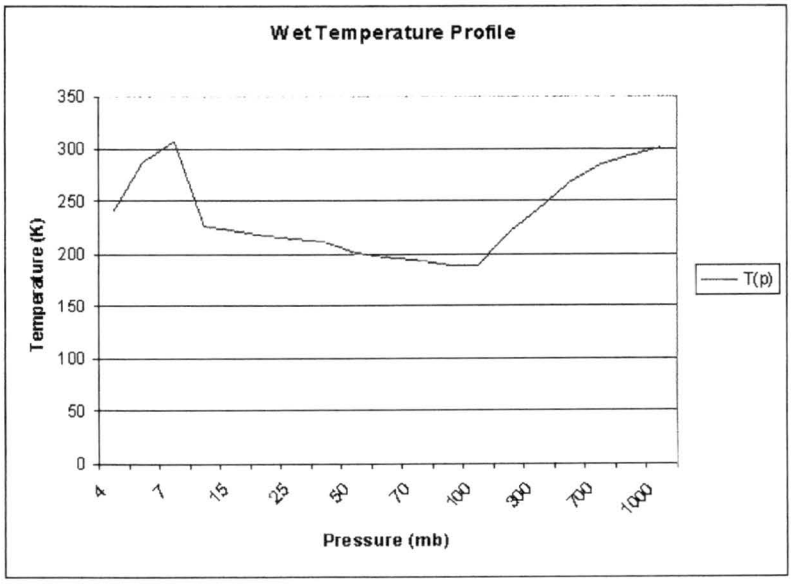

Figure 5.4: The temperature profile for the "wet" case.

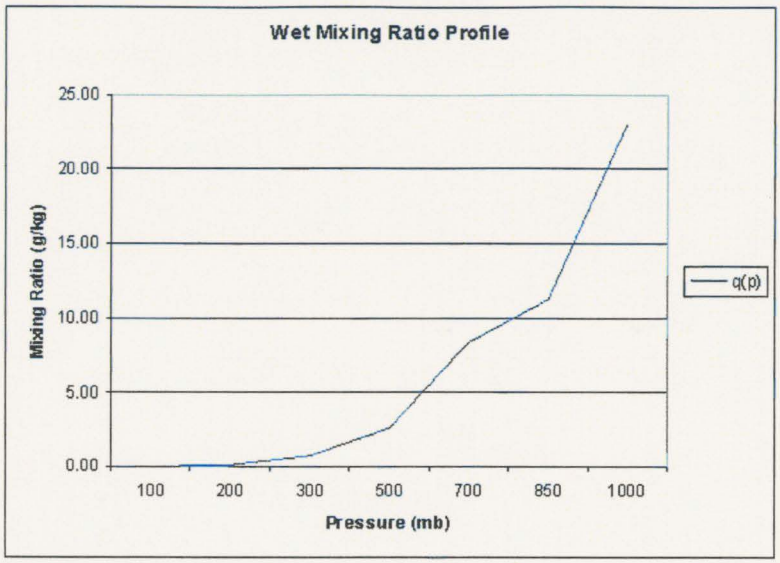

Figure 5.5: The mixing ratio profile for the "wet" case.

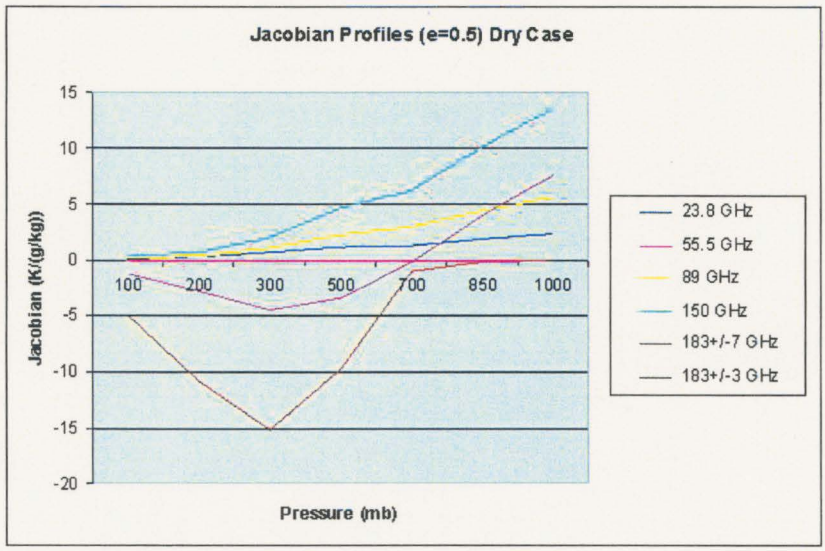

Figure 5.6: The Jacobian vertical profiles for six frequencies (23.8, 55.5, 89, 150, 183+/-7GHz, and 183+/-3GHz for the dry atmospheric case with an emissivity of 0.5.

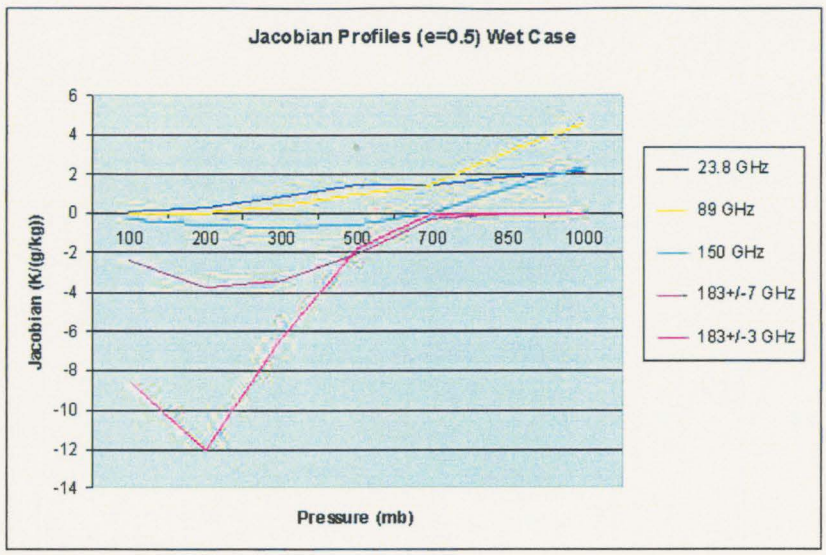

Figure 5.7: The Jacobian vertical profiles for five frequencies (23.8, 89, 150, 183+/-7GHz, and 183+/-3GHz for the wet atmospheric case with an emissivity of 0.5.

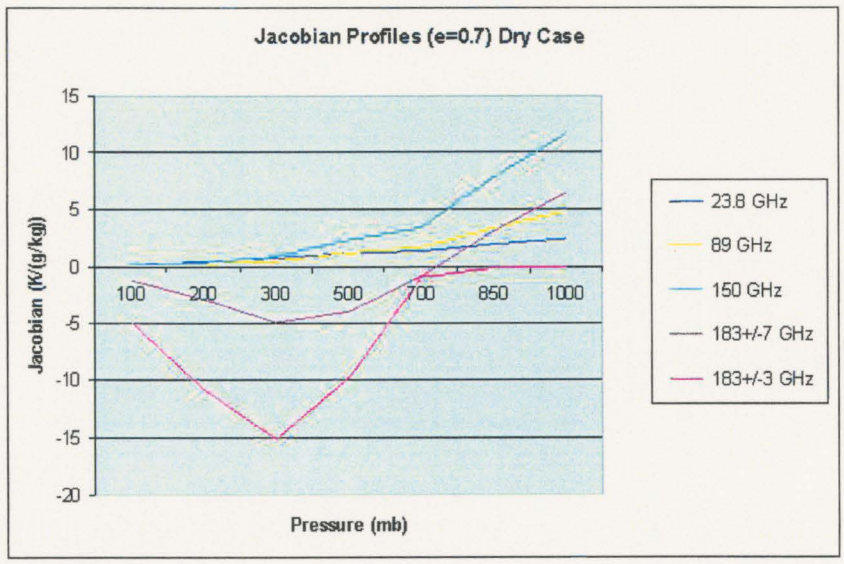

Figure 5.8: The Jacobian vertical profiles for five frequencies (23.8, 89, 150, 183+/-7GHz, and 183+/-3GHz for the dry atmospheric case with an emissivity of 0.7.

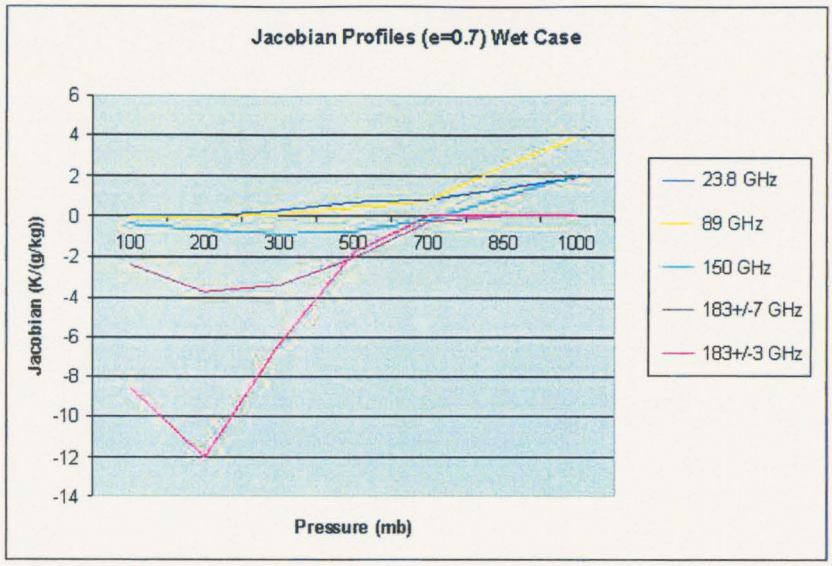

Figure 5.9: The Jacobian vertical profiles for five frequencies (23.8, 89, 150, 183+/-7GHz, and 183+/-3GHz for the wet atmospheric case with an emissivity of 0.7.

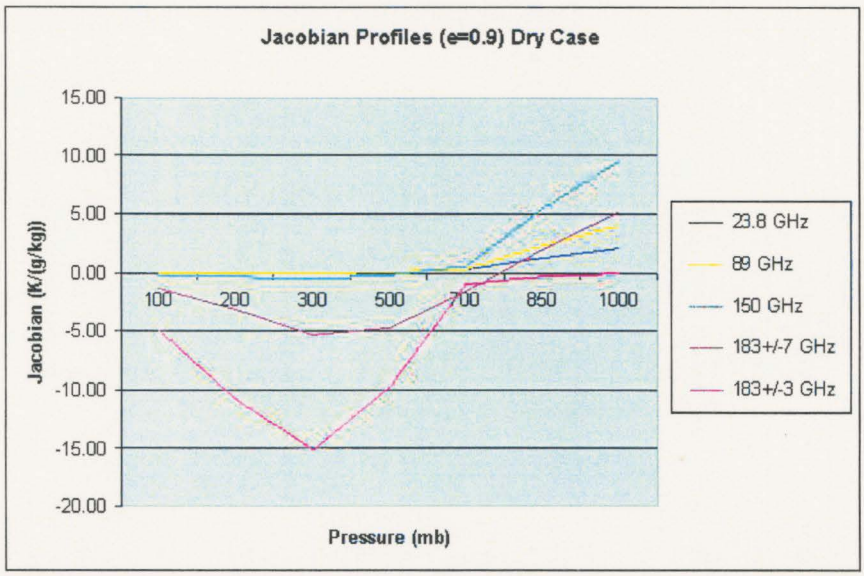

Figure 5.10: The Jacobian vertical profiles for five frequencies (23.8, 89, 150, 183+/-7GHz, and 183+/-3GHz for the dry atmospheric case with an emissivity of 0.9.

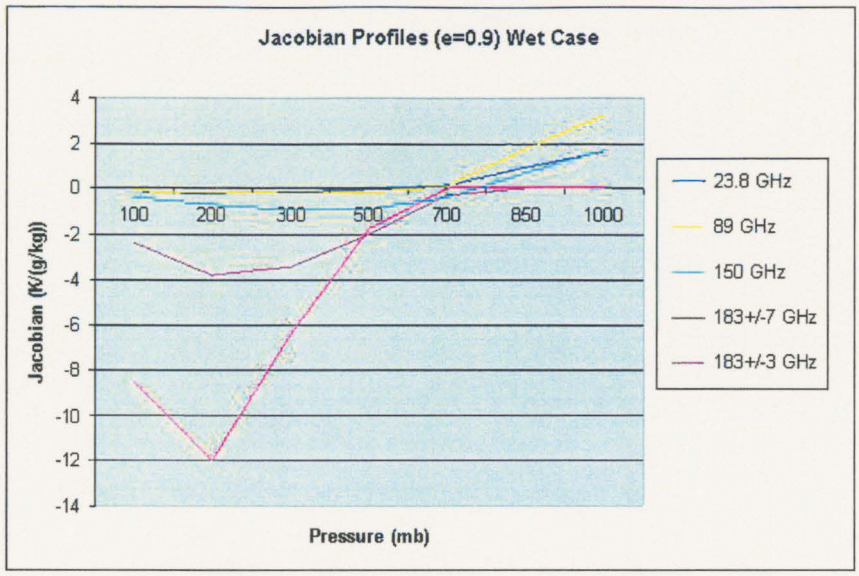

Figure 5.11: The Jacobian vertical profiles for five frequencies (23.8, 89, 150, 183+/-7GHz, and 183+/-3GHz for the wet atmospheric case with an emissivity of 0.9.

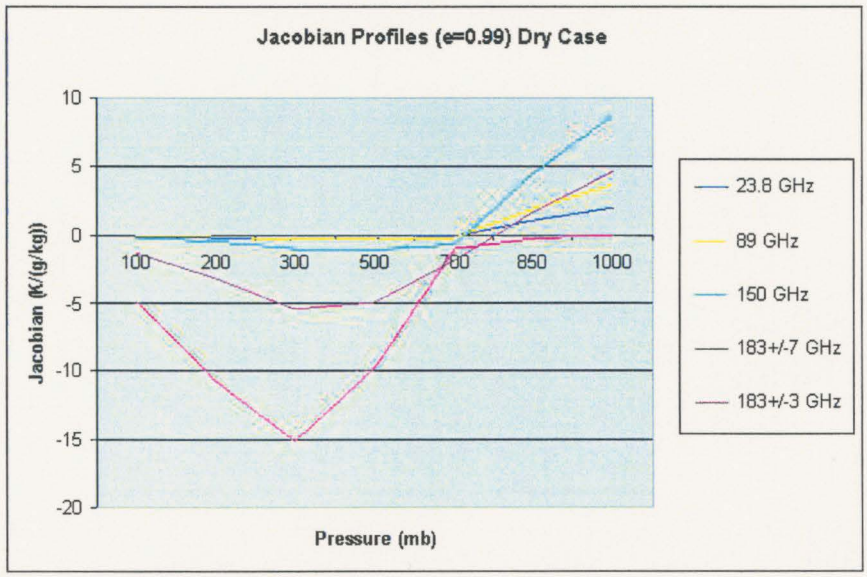

Figure 5.12: The Jacobian vertical profiles for five frequencies (23.8, 89, 150, 183+/-7GHz, and 183+/-3GHz for the dry atmospheric case with an emissivity of 0.99.

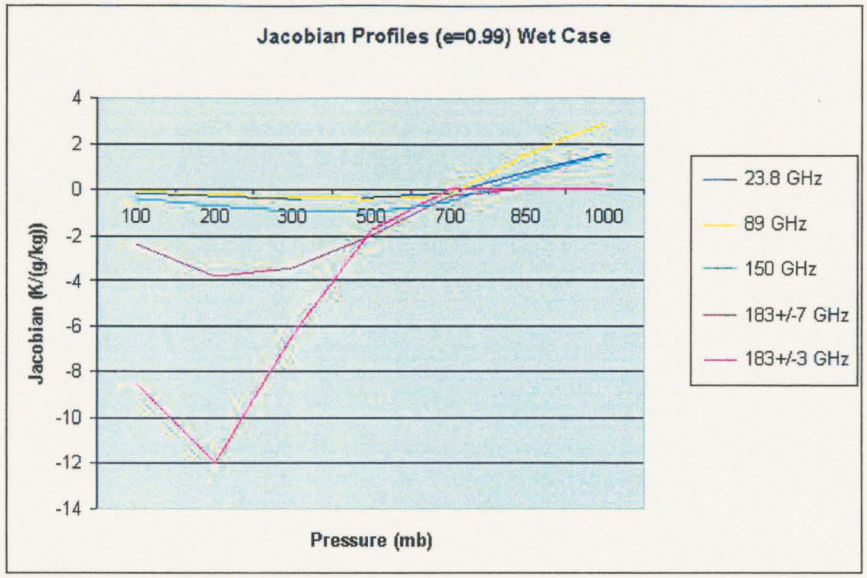

Figure 5.13: The Jacobian vertical profiles for five frequencies (23.8, 89, 150, 183+/-7GHz, and 183+/-3GHz for the wet atmospheric case with an emissivity of 0.99.

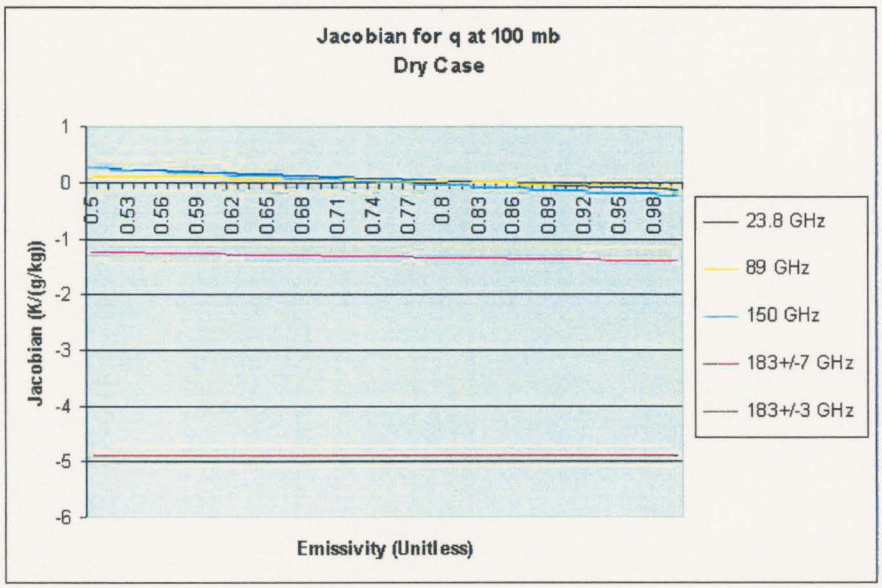

Figure 5.14: The change in the Jacobian for five frequencies (23.8, 89, 150, 183+/-7GHz, and 183+/-3GHz) at 100 mb as the emissivity is increased from 0.5 to 1.0 for the dry case.

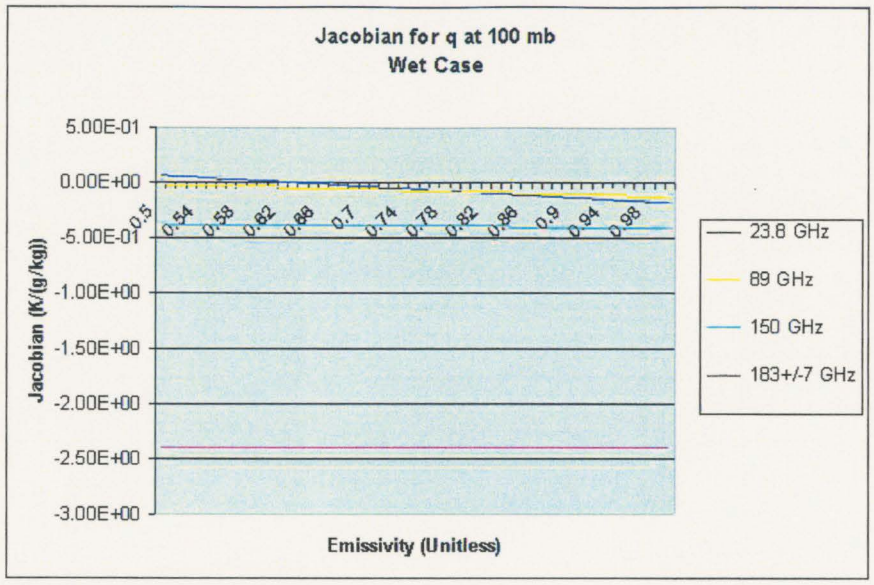

Figure 5.15: The change in the Jacobian for four frequencies (23.8, 89, 150, and 183+/-7GHz) at 100 mb as the emissivity is increased from 0.5 to 1.0 for the wet case.

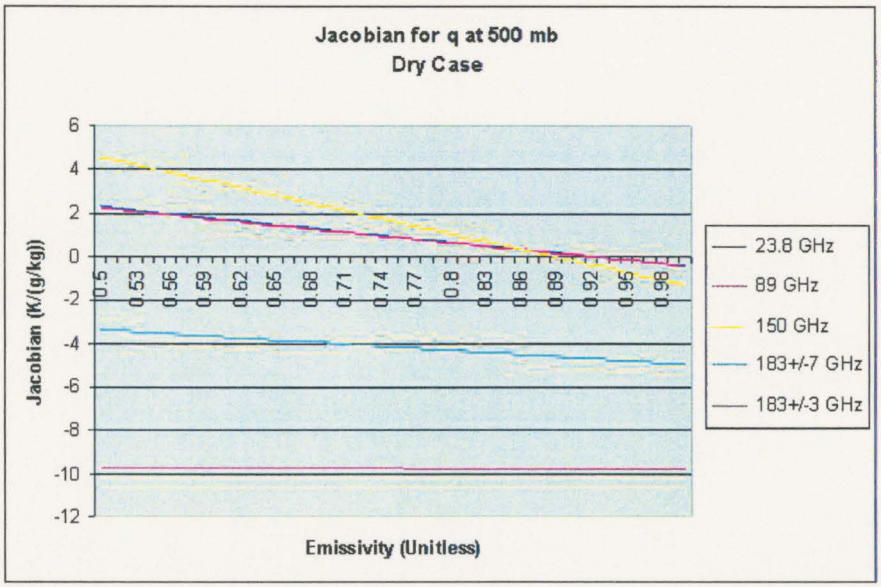

Figure 5.16: The change in the Jacobian for four frequencies (23.8, 89, 150, and 183+/-7GHz) at 500 mb as the emissivity is increased from 0.5 to 1.0 for the dry case.

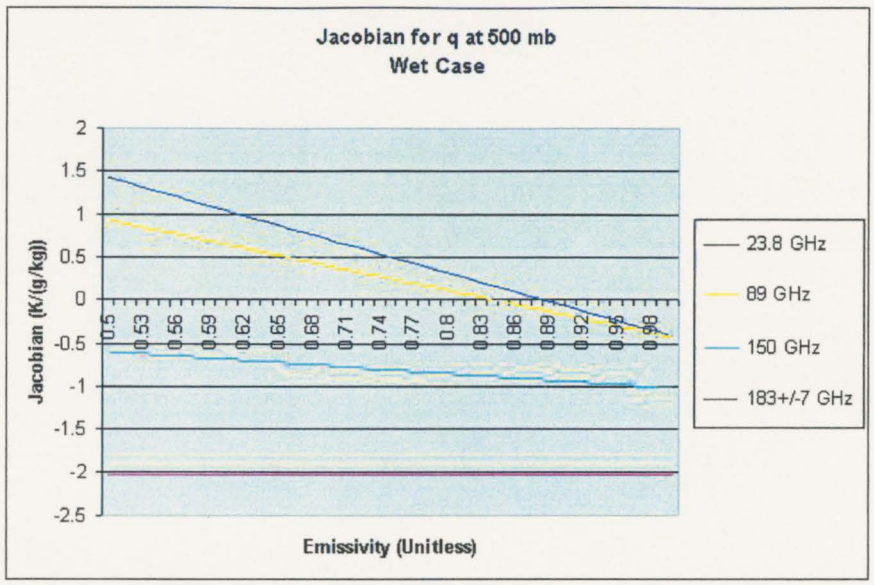

Figure 5.17: The change in the Jacobian for four frequencies (23.8, 89, 150, and 183+/-7GHz) at 500 mb as the emissivity is increased from 0.5 to 1.0 for the wet case.

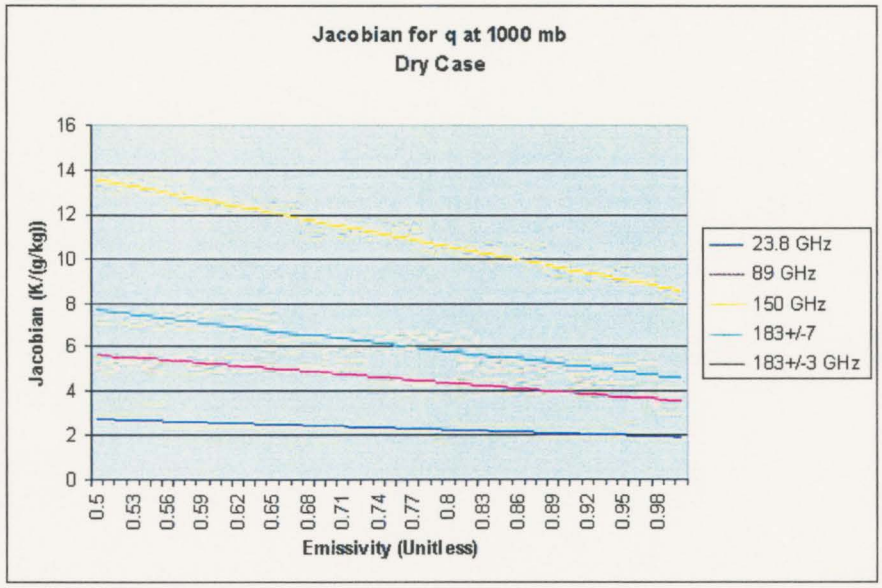

Figure 5.18: The change in the Jacobian for four frequencies (23.8, 89, 150, and 183+/-7GHz) at 1000 mb as the emissivity is increased from 0.5 to 1.0 for the dry case.

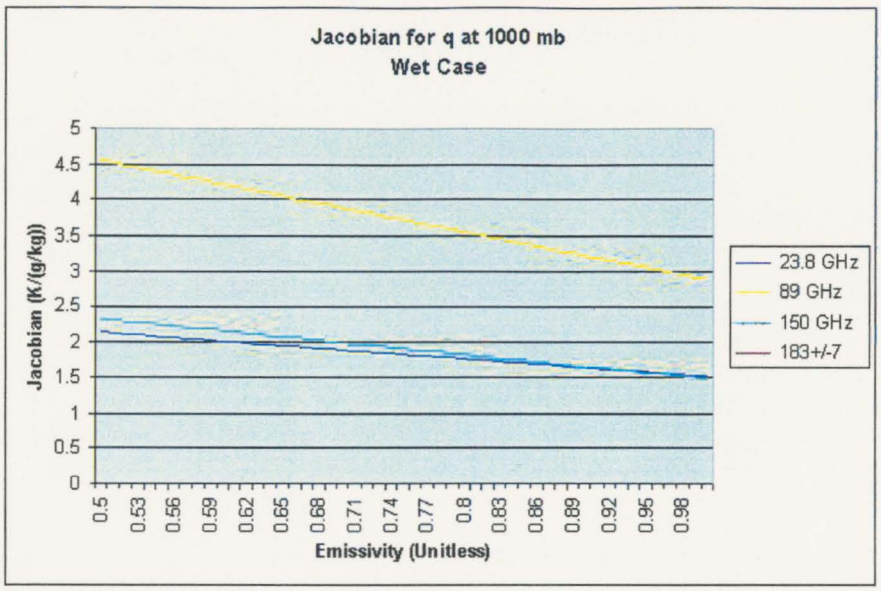

Figure 5.19: The change in the Jacobian for four frequencies (23.8, 89, 150, and 183+/-7GHz) at 1000 mb as the emissivity is increased from 0.5 to 1.0 for the wet case.

Channel (freq in GHz)	NEΔT (spec)	NEΔT (measured)
1 (23.8)	0.30	0.211
2 (31.4)	0.30	0.265
3 (50.3)	0.40	0.219
4 (52.8)	0.25	0.143
5 (53.59)	0.25	0.148
6 (54.4)	0.25	0.154
7 (54.94)	0.25	0.132
8 (55.5)	0.25	0.141
9 (57.29)	0.25	0.236
10 (~57.29)	0.40	0.250
11 (~57.29)	0.40	0.280
12 (~57.29)	0.60	0.399
13 (~57.29)	0.80	0.539
14 (~57.29)	1.20	0.914
15 (89.0)	0.50	0.165
16 (89.0)	0.37	0.37
17 (150.0)	0.84	0.84
18 (183.31+/-1.00)	1.06	1.06
19 (183.31+/-1.00)	0.70	0.70
20 (183.31+/-1.00)	0.60	0.60

Figure 5.20: The corresponding NEΔT values for all AMSU channels (data taken from NOAA KLM Users Guide: Goodrum et al, 1999).

CHAPTER 6: RESULTS AND CONCLUSIONS

6.1 Results

Examining the analytical Jacobian serves as a way to determine the ability of the retrieval to detect water vapor throughout a vertical column. Several scenarios were used to investigate how this Jacobian is affected by changes in atmospheric and surface conditions. This was a test to check that the retrieval could still detect water vapor with some skill under real world simulations. The Jacobian analysis proves that water vapor can be measured throughout the column, and thus gives basis for running and validating the retrieval. This analysis technique can be applied to any satellite platform and is a crucial and fundamental step to take before analyzing results from any retrieval. Once this analysis has been performed, and the state vector has been determined to be detectable over the time and spatial regions of interest, then the retrieval may be run and validated.

In order to test the accuracy and validity of the C1DOE TPW, the retrieval was run over a 10-day period under non-precipitating conditions for September 21 – September 30, 2003, and then compared with similar data from both GPS receivers and radiosondes. In order to isolate the retrieval bias from the first guess bias, the retrieval was run with a radiosonde first guess. DISCLAIMER: Due to the extraordinarily accurate first guess, Gaussian noise was added to the first guess in order to obtain a reasonable upper bound on how the retrieval can ultimately

perform. The radiosonde match-up dataset was created by finding launches that were within a 50-km radius of the satellite footprint, and launched within a two-hour window of the satellite overpass. The GPS match-ups were compiled over the United States by matching data taken within 30 minutes of a pass-over and were typically within 30 kilometers of the center of the satellite footprint.

The retrieved TPW was then plotted against the radiosonde TPW in order to produce Figure 6.2. There were 555 radiosonde match-up points spread all across the globe (see Figure 6.1). This plot serves as a mythological best estimate for how the retrieval can perform, due to the fact that radiosonde data was used as a first guess. Essentially, this shows how the retrieval physics is performing, given a highly accurate first guess of temperature and water vapor profiles.

Noise was added to the first guess of the mixing ratio profile before it was run through the retrieval in order to show a more realistic spread. The noise was added similarly to Deblonde, 2000. A Gaussian distribution was created with a standard deviation of 10% of the first guess for mixing ratio, and then randomly added and subtracted from all mixing ratio first guess data.

Examining Figure 6.2 shows that the retrieval is in fairly good agreement with the radiosonde first guess data, with the exception of the upper TPW region (above 40 mm). There appears to be a low bias in this upper TPW regime, and some of this can be accredited to coastline data points. This is caused (most likely) by the cold ocean background contaminating the land scenes and causing the satellite to see less water vapor than the radiosondes. The Jacobians for land emissivity signatures are much smaller than for ocean backgrounds, particularly in high

moisture regions. If the retrieval sees an ocean scene where a land scene exists, the user will associate the ocean scene with a lower sensitivity to water vapor. In order to explore the validity of faulting coastline points, two separate plots were made: a plot of only coastline data points from the match-up, and a plot of only non-coastline data points. Figure 6.3 is a plot of the retrieval versus radiosonde TPW amounts for only coastline data points. As can be seen, the upper TPW region still has a low bias with respect to the radiosondes. The lower TPW values still seem to correspond fairly well with the radiosonde data, however there is a very slight high bias below 25 mm. Figure 6.4 is a plot of the retrieval versus radiosonde TPW for only non-coastline data points. This figure serves as a more confident measure that a bias is contaminating the coastline points. These non-coastline data points have a very even distribution and seem to have only random scatter as opposed to a systematic bias.

Part of this bias may also be caused by the emissivity first guess, which comes from the Microwave Emissivity Model (MEM). The MEM has notoriously had trouble resolving emissivities near coastlines, and can also be causing ocean emissivity signatures over land regions. The retrieval version of C1DOE used in the present study does not have knowledge of clouds, therefore it is not able to distinguish between cloudy and non-cloudy pixels. This may also serve as a source of bias in the retrieval as well.

The retrieved TPW was then plotted against the GPS TPW in order to produce Figure 6.5. All of the latitude and longitude points where plotted on a global map, and were then matched to corresponding GPS stations. There were 26 GPS match-

up points spread over the east and western coasts of the United States, as well as over Alaska, Hawaii, and Puerto Rico. The agreement between the retrieval and the GPS TPW amounts is not quite as good as in the radiosonde case. This is partially due to the significantly smaller GPS TPW database as compared to the radiosonde stations. However some of the bias comes from the dislocation between the retrieval and the radiosonde data. For example, some of the higher TPW cases come from the island of Kauai, Hawaii. The GPS station at Kokole Point is on the west side of the island, which is notorious for being the wettest area in the United States of America. The retrieval, however, covers the southeast side of the island near the area of Lihue, which is significantly drier. September 2003 showed near normal monthly precipitation at Lihue of 2.73 inches, whereas the western side of the island reported anywhere from 190 to 213 % of average with the station at Kokee reporting 6.64 inches of precipitation for the month. Point Barrow was another trouble point, as the retrieval was disjoint from the GPS site by about 30 kilometers. Both the retrieval and the GPS site were located on or near the coast in both cases, which also causes bias due to the first guess and ocean contamination discussed earlier.

Having a very solid knowledge about the nature of the data points that were fed in to the retrieval served to be very valuable. Had the match-up data points not been investigated, this co-location bias may not have been uncovered. This could have led to believing that the data had another systematic bias that needed to be detected.

The RMS differences between the radiosondes and the retrieval were plotted and can be seen in Figure 6.6. This shows the same general trend as Figure 6.2, and provides an easier way to detect bias in the retrieval. As can be seen, most of the difference between the two methods lies under 10 mm.

Figure 6.7 shows a histogram of the land emissivity values. This not only serves as a sanity check that these retrievals were in fact done over land regions, but also is a good indicator of the location in the emissivity spectrum where the data is most concentrated. As can be seen, most of the data comes from areas with an emissivity greater than 0.9. Most seem to be concentrated about the e=0.95 line, which gives confidence that these are truly land retrievals.

6.2 Conclusions

Bias detection and removal was an important first step for ensuring that the retrieval would produce accurate and meaningful results. The antenna pattern correction was developed and implemented, and showed not only improved radiances, but also the effect of the correction on the state vector elements themselves (Nielsen et al., 2005). This work exposed the need to be aware of all of the calibration and bias removal that has been performed by the instrument manufacturer. Many scientists have used this data without applying a sidelobe correction, degrading the value of their data. This occurs simply because some users assume that these tests have been done without actually performing a quality control check.

The analytical Jacobian proved to be a very valuable tool for diagnosing the information content of the retrieval. Examining the vertical profiles of the Jacobian with predetermined frequencies highlights the channels that are best suited for retrieving particular parameters. This also shows problem areas where there may not be enough information to perform an adequate retrieval, allowing the user to reconsider channel configurations. Due to the fact that the physics is essentially consistent between satellite platforms, this information can be easily used for channel selections on other space-borne microwave radiometers, such as ATMS (Advanced Technology Microwave Sounder) or CMIS (Conical Scanning Microwave Imager/Sounder).

The Jacobian research conducted on the C1DOE showed that the profiler channels (183 GHz) are able to provide excellent middle and upper tropospheric water vapor knowledge at any emissivity. The imager channels do lose a considerable amount of sensitivity as the emissivity begins to approach unity, however most of the channels still retain signal that is above the instrument noise, allowing lower tropospheric water vapor to be retrieved. Strong dependence of the Jacobian to emissivity in atmospheric layers near the surface does present a problem that will hopefully be overcome in the immediate future.

Running the retrieval with a highly accurate first guess enabled the detection of bias in the forward model. It also served as an upper bound as to how well the retrieval can perform. This is important because it shows whether or not the C1DOE will be capable of retrieving water vapor with any accuracy. The bulk of the RMS differences between the radiosondes and the retrieval were below 5mm,

which corresponds to a total difference of less than 20% in most cases. This shows a lot of promise for this retrieval, especially when considering the areas of improvement that can easily be made (see Section 6.3). The GPS match-up showed good results for lower values of TPW, however, it underestimated the higher values by 20-35%. This can be explained when considering the distance between the GPS station and the footprint of the retrieval as discussed in Section 6.1. These upper TPW regions are also coastline retrievals, thereby introducing the bias previously discussed in Section 6.1.

The C1DOE retrieval underwent a calibration and bias removal procedure that involved an antenna pattern correction for the AMSU-B instrument that may also be applied to other microwave satellite platforms. The analytical Jacobian was examined and the retrieval was determined to be able to detect tropospheric water vapor with decent skill. The C1DOE was run with a highly accurate first guess and was validated against radiosondes and GPS TPW data. Validation exposed a systematic bias with the retrieval. Several reasons for this bias were discussed. The TPW values agreed within 20% when compared to radiosondes, and within 20-35% for GPS. These results give confidence that AMSU can detect TPW over land for both weather forecasting and for climate studies. The current capabilities may be improved further once bias sources are dealt with satisfactorily.

6.3 Future Work

As with any retrieval scheme, numerous ways exist in order to improve the validity of the results produced. A liquid and ice cloud module needs to be implemented as the current retrieval has no knowledge of clouds. This would make cloud screening possible, as well as providing an improved vertical profile of mixing ratio and temperature. A better first guess for emissivity is also needed, and will come from a composite of retrieved emissivities instead of the MEM. Exploration in to better covariance matrices is needed as well as looking in to A-matrix metrics.

The first guess for water vapor will come from GDAS (Global Data Assimilation System) as to provide a retrieval that is not based on an impossible first guess scenario. This first guess scenario is impossible due to the fact that the radiosonde match-up dataset had radiosonde launches that occurred after the satellite overpass. In addition, the GDAS first guess will be able to provide data over a larger land area. The retrieval should also be more heavily validated against the GPS TPW data. Once the retrieval is not dependent on a radiosonde match-up dataset that eliminated retrievals over the Great Plains of the United States of America, GPS validation will become easier and much more meaningful.

GPS data may also be an attractive choice for a first guess of TPW in future retrievals, especially with GPS occultation data becoming more readily available. GPS TPW data has been known to be of high accuracy, however, there are other ways that GPS will be able to contribute to first guess fields of the C1DOE as well.

Radio occultation data may be able to provide a water vapor profile from 6 – 24 km above earth's surface. These data will serve as an accurate detection of the tropopause height due to bending angle geometry. For these reasons, GPS will prove to be a valuable constraint on the C1DOE retrieval.

Once these things have been performed, the retrieval will be better suited to retrieve water vapor over land. This new land retrieval method will then be ready to be applied to aid synoptic weather forecasting worldwide, as well as serving to create a more accurate climate record. Its impact on global data assimilation will be determined and will most likely improve water vapor fields over land, especially under cloudy conditions.

The calibration and Jacobian analysis procedures will prove to be valuable to all users of satellite data. The antenna pattern correction will serve as a necessary component to any microwave retrieval. Jacobian analysis will enable satellite data users to determine a retrieval's capability to retrieve state vector parameters at varying frequencies under changing atmospheric conditions. It will also serve as a roadmap to sensor design and channelization for many forms of remote sensing platforms that have yet to be developed.

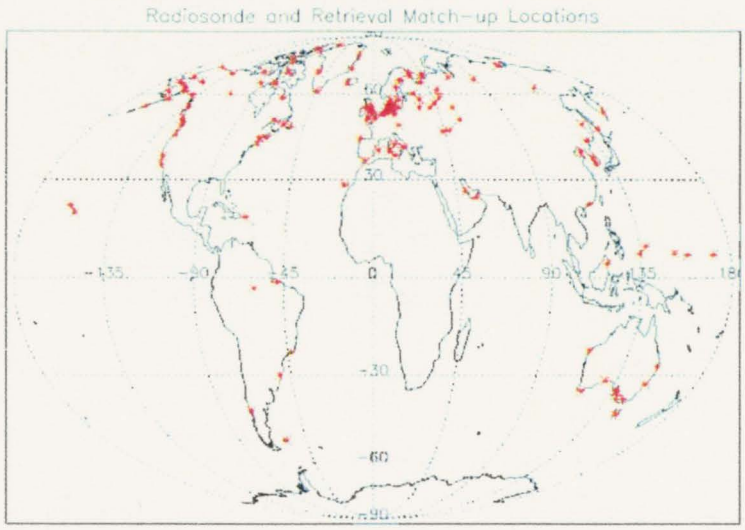

Figure 6.1: A global map of the radiosonde and retrieval match-up data locations.

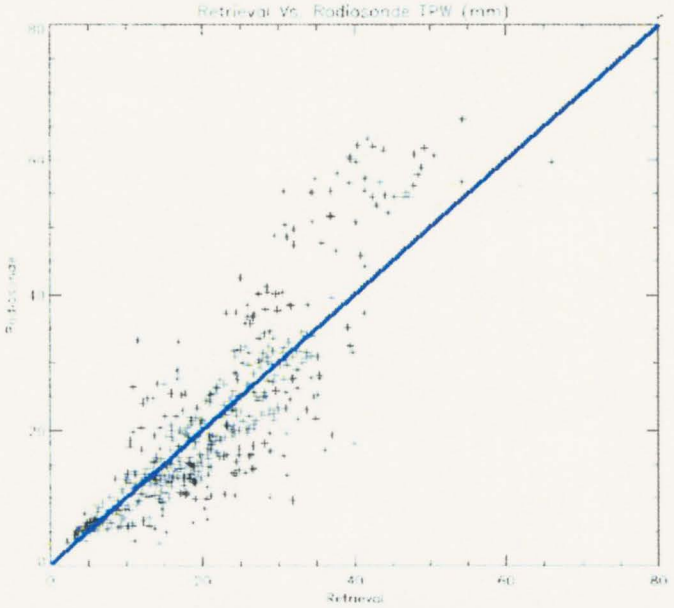

Figure 6.2: A plot of the radiosonde TPW versus the retrieved TPW. Units are in millimeters (mm).

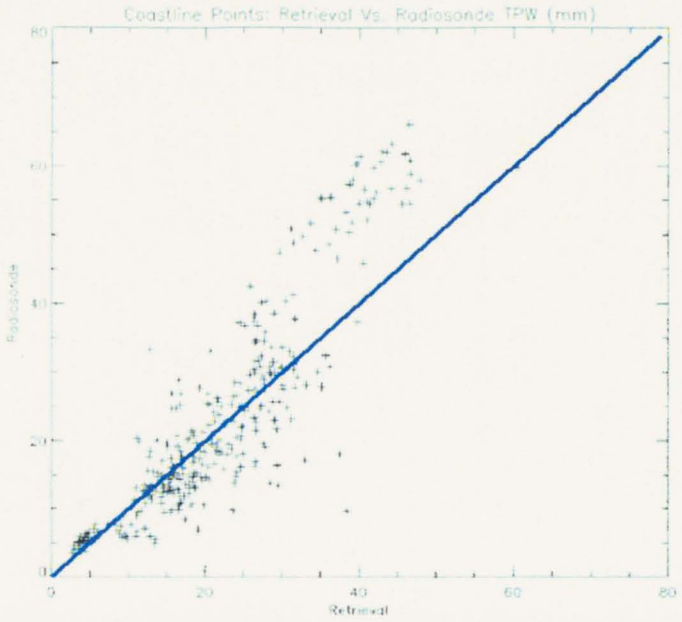

Figure 6.3: A plot of the radiosonde TPW versus the retrieved TPW for only coastline data points. Units are in millimeters (mm).

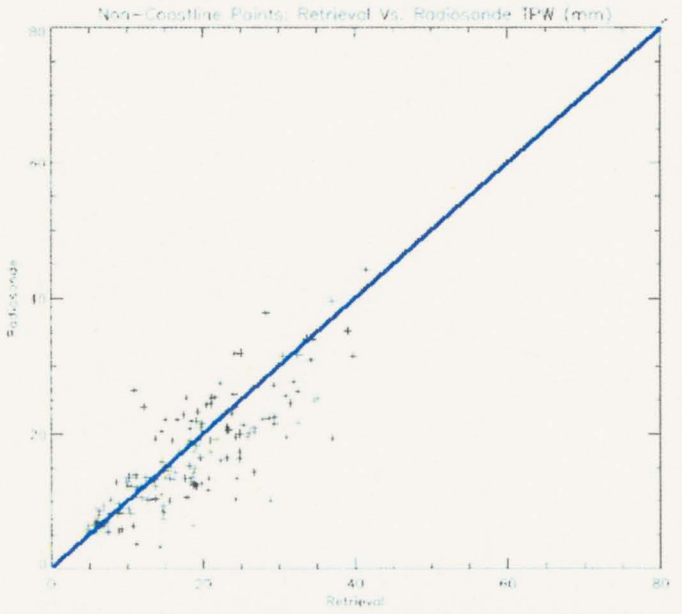

Figure 6.4: A plot of the radiosonde TPW versus the retrieved TPW for only non-coastline data points. Units are in millimeters (mm).

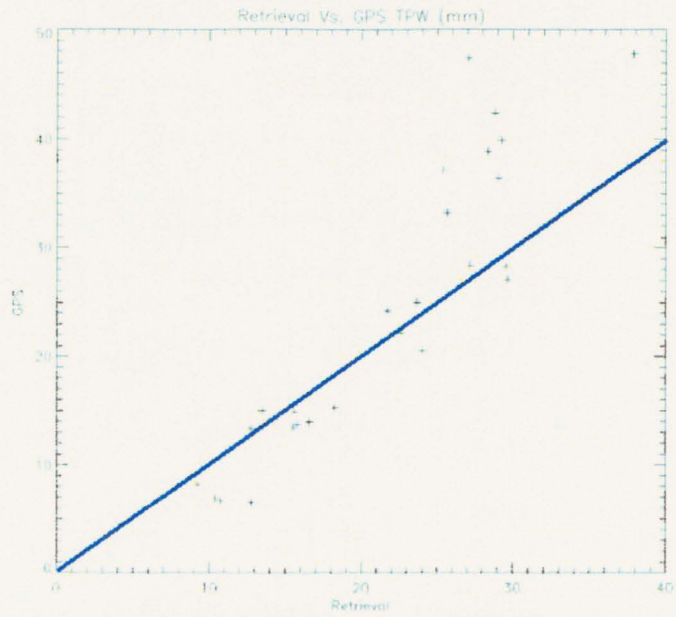

Figure 6.5: A plot of the GPS TPW versus the retrieved TPW. Units are in millimeters (mm).

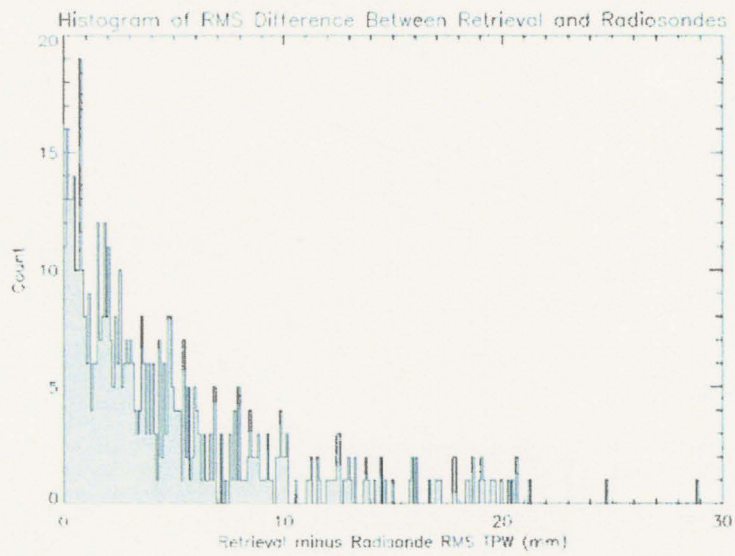

Figure 6.6: A plot of the radiosonde and retrieval RMS difference (in mm).

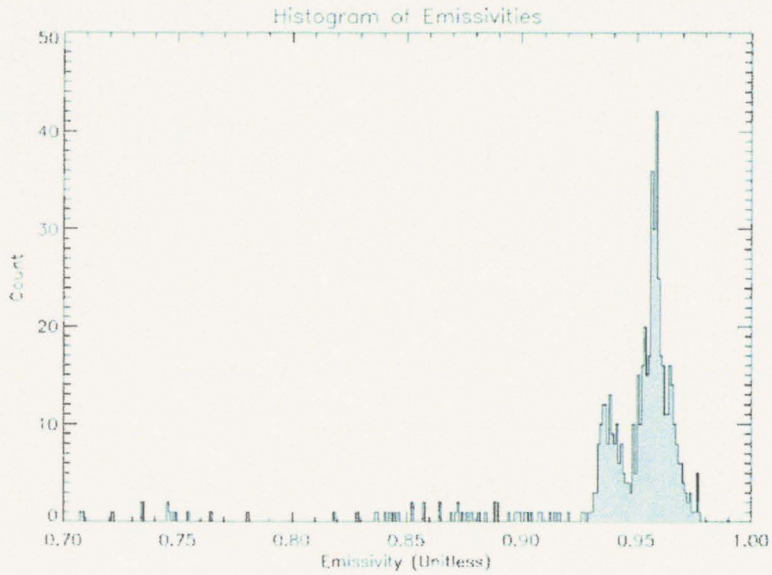

Figure 6.7: A histogram of the retrieved emissivities.

REFERENCES

Bevis, M., Businger, S., Herring, T. A., Rocken, C., Anthes, R. A., and Ware, R. H., 1992: GPS Meteorology: Remote Sensing of Atmospheric Water Vapor Using the Global Positioning System. *J. Geophys. Res.*, **97,**, 15787-15801.

Bevis, M., Businger, S., Chiswell, S., Herring, T., Anthes, R., Rocken, C., and Ware, R., 1993: GPS Meteorology: Mapping Zenith Wet Delays onto Precipitable Water. *J. App. Meteorol.*, **33,** 379-386.

Chandrasekar, S., 1960: *Radiative Transfer.* Dover Publications Inc., New York, 393 pp.

Deblonde, G., 2000: Variational Retrievals Using SSM/I and SSM/T-2 Brightness Temperatures in Clear and Cloudly Situations. *J. Atmos. Oceanic Technol.*, **18,** 559-576.

Deeter, M. N. and K. F. Evans, 1998: A hybrid Eddington-single scattering radiative transfer model for computing radiances from thermally emitting atmospheres. *J. Quant. Spectosc. Radiat. Transfer*, 60, 635-648.

Engelen, R. J. and G. L. Stephens, 1999: Characterization of water-vapour retrievals from TOVS/HIRS and SSM/T-2 measurements. *Q. J. R. Meteor. Soc.*, 125, 331–351.

Forsythe, J. M., Jones, A. S., and Vonder Haar, T. H., 2004: Water Vapor Profile Retrievals From Satellite Microwave Sounding Instruments. *Proceedings of the 13th Conference on Satellite Meteorology and Oceanography,* Norfolk, VA, Amer.Meteor. Soc.

Goodrum, G., K. B. Kidwell, and W. Winston, Eds., 1999: NOAA KLM User's Guide. National Oceanic and Atmospheric Administration

Hewison, T. J., and R. Saunders, 1996: Measurements of the AMSU-B antenna pattern. IEEE Trans. Geosci. Remote Sens., 31, 405-412

Jacobsen, M. Z., 1999: *Fundamentals of Atmospheric Modeling.* Cambridge University Press, 656 pp.

Jet Propulsion Laboratory, 2000: AIRS Project: Algorithm Theoretical Basis Document: Microwave Instruments, Version 2.1, pp41-46

Jones, A. S., 1989: Microwave Remote Sensing of Liquid Water and Surfact Emittance Over Land Regions. M. S. thesis, Department of Atmospheric Science, Colorado State University, 145 pp.

Jones, A. S. and T. V. Vonder Haar, 2002: A dynamic parallel data-computing environment for cross-sensor satellite data merger and scientific analysis. *J. Atmos. Oceanic Technol.*, 19, 1307–1317.

Jones, A. S., Forsythe, J. M., and Vonder Haar, T. H., 2004: Retrieval of Global Microwave Surface Emissivity Over Land. *Proceedings of the 13th Conference on Satellite Meteorology and Oceanography,* Norfolk, VA, Amer. Meteor. Soc.

Kidder, S.Q. and T. V. Vonder Haar, 1995: *Satellite Meteorology: An Introduction.* Academic Press, 466 pp.

Kiehl, J. T. and Trenberth, K. E., 1997: Earth's annual global mean energy budget, *Bull. Amer. Meteorol. Soc.*, **78,** 197-208.

Leibe, H. J. and G. A. Hufford, 1993: Models for atmospheric refractivity and radio-wave propagation at frequencies below 1 THZ. *Int. J. Infrared and Millimeter Waves*, 77, 437–471.

McKague, D. S., R. J. Engelen, J. M. Forsythe, S. Q. Kidder, and T. H. Vonder Haar, 2001: An optimal estimation algorithm for water vapor profiling using AMSU. *Proceedings of the 11th Conference on Satellite Meteorology and Oceanography*, 633–636.

McKague, D. S., J. M. Forsythe, A. S. Jones, S. Q. Kidder, and T. H. Vonder Haar, 2003: A passive microwave optimal-estimation algorithm for near real-time water vapor profiling. *Proceedings of the 11th Conference on Satellite Meteorology and Oceanography.*

Meyer, C. L., 2004: Forecasting Rain Events in the Southern Great Plains Using GPS Total Precipitable Water Amounts. M.S. thesis, Department of Atmospheric Science, Colorado State University, 114 pp.

Mo, T., 1999: AMSU-A antenna pattern corrections. IEEE Trans. Geosci. Remote Sens., 37, 103-112

The NASA Water Vapor Project (NVAP), cited 2005: NVAP Data Sets. [Available online at http://eosweb.larc.nasa.gov/PRODOCS/nvap/table_nvap.html]

Nielsen, M. J., Jones, A. S., Forsythe, J. M., and Vonder Haar, T. H., 2004: Effect of Antenna Pattern Corrections on AMSU-B Radiances. *Proceedings of the 13th Conference on Satellite Meteorology and Oceanography,* Norfolk, VA, Amer. Meteor. Soc.

Nielsen, M. J., Stephens, P. J., Jones, A. S., Forsythe, J. M., Kessler, R. W., Vonder Haar, T. H., 2005: AMSU-B Antenna Pattern Corrections. Submitted to *J. Atmos. Oceanic Technol.*

NOAA Forecast Systems Laboratory GPS-Met Observing Systems Branch, cited 2005: NOAA/FSL Ground-Based GPS Integrated Precipitable Water Vapor Real Time Water Vapor Intereface. [Available online at http://gpsmet.noaa.gov]

Randel, D., Vonder Haar, T. H., Ringerud, M., Stephens, G., Greenwald, T., and Combs, C., 1996: A New Global Water Vapor Dataset. *Bull amer. Meteorol. Soc.*, **77,** 1233-1246.

Rocken, C., Ware, R. H., Van Hove, T., Solheim, F., Alber, C., Johnson, J., and Bevis, M. G., 1993: Sensing Atmospheric Water Vapor with the Global Positioning System. *Geophys. Res. Lett.*, **20,** 2631-2634.

Rodgers, C. D., 1976: Retrieval of atmospheric temperature and composition from remote measurements of thermal radiation. *Rev. Geophys. Space Phys.*, 14, 609–624.

Rodgers, C. D., 2000: *Inverse Methods for Atmospheric Sounding.* World Scientific Publishing Co., 238 pp.

Rosenkranz, P. W., 2001: Retrieval of temperature and moisture profiles from AMSU-A and AMSU-B measurements. *IEEE Trans. Geosci. Rem. Sens.*, 39, 2429–2435.

Rothacher, M., 2004: The GPS/GNSS Observation Equation and Data Processing. *Atmospheric Remote Sensing Using the Global Positioning System Colloquim*, Boulder, CO, NCAR/UCAR.

Ruston, B. C., 2004: Characteristics of Summertime Microwave Land Emissivity Over the Conterminous United States. Ph.D dissertation, Colorado State University, 126 pp.

Saunders, R.W., Hewison, T.J., Atkinson, N.C., and Stringer, S.J., 1995: The radiometric characterization of AMSU-B. *IEEE Trans. Microwave Theory Tech.*, vol. 43, pp. 760-771

Stephens, G. L., 1994: *Remote Sensing of the Lower Atmosphere.* Oxford University Press, 523 pp.

Ulaby, F. T., Moore, R. K., Fung, A. K., 1981: *Microwave Remote Sensing: Active and Passive*. Artech House, 456 pp.

Weng, F., Banghua, Y., and Grody, N. 2001: A Microwave Land Emissivity Model, *Journal of Geophysical Research.,* Vol. 106, No.D17, Pages 20,115-20,123